Geological Society of America Bulletin

Late tectonic and metamorphic evolution of the Piedmont accretionary wedge (Queyras Schistes lustrés, western Alps): Evidences for tilting during Alpine collision

Stéphane Schwartz, Pierre Tricart, Jean-Marc Lardeaux, Stéphane Guillot and Olivier Vidal

Notes

THE
GEOLOGICAL
SOCIETY
OF AMERICA

Late tectonic and metamorphic evolution of the Piedmont accretionary wedge (Queyras Schistes lustrés, western Alps): Evidences for tilting during Alpine collision

Stéphane Schwartz[†]
Laboratoire de Géophysique Interne et Tectonophysique, Université Grenoble 1, CNRS/UJF, F-38041 Grenoble, Cedex 9, France

Pierre Tricart
Laboratoire de Géodynamique des Chaînes Alpines, Université Grenoble 1, CNRS/UJF, F-38041 Grenoble, Cedex 9, France

Jean-Marc Lardeaux
Géosciences Azur, Université de Nice Sophia Antipolis, CNRS, F-06108 Nice, Cedex 02, France

Stéphane Guillot
Olivier Vidal
LGCA, Université Grenoble 1, CNRS/UJF, F-38041 Grenoble, Cedex 9, France

ABSTRACT

This paper addresses the contribution of extension in the upper crust during syncollisional exhumation of subducted material. We present structural data based on the analysis of ductile, brittle-ductile, and brittle deformation features in meta-pelitic schists and meta-basalts from the Schistes lustrés nappe stack in the Piedmont zone of the western Alps. To link the structures with synkinematic pressure and temperature estimates, geothermobarometry was performed using fluid inclusion investigation in quartz together with temperature estimations based on metamorphic chlorite composition. Samples used for geothermobarometry were collected taking into account the structural framework within veins associated with extensional structures observed at the regional scale. The early generation of veins associated with boudinage occurred at 415–345 °C and 6–2.5 kbar, and subsequent incipient normal faulting occurred at temperatures of 315–235 °C and pressures <1.7 kbar. The transition from ductile to brittle extension occurred between ca. 27 Ma and ca. 10 Ma. These results indicate a continuous extension in the upper crust during exhumation and continuous deformation associated with regional-scale tilting of the exhumed Schistes lustrés tectonic pile. The extensional tectonic regime in greenschist-facies conditions remains active today in most of the internal Alpine zones as the Alpine collision continues.

Keywords: western Alps, Schistes lustrés unit, deformation sequence, tectonic analysis, fluid inclusion, final exhumation.

INTRODUCTION

Syncollision extension has been recognized for more than a decade (e.g., Platt, 1987; Molnar and Lyon-Caen, 1988) as a major process controlling the structural evolution of Alpine-type mountain ranges along converging plate boundaries. Extension is often associated with the exhumation of metamorphic units in the inner zones of orogenic belts (Malavieille et al., 1990; Hodges et al., 1992; Jolivet et al., 1996; Ring et al., 1999). The nature of the forces driving syncollisional extension remains debated due to the variety of documented tectonic situations and suitable interpretative models, including shallow extension assisted by deep tectonic underplating, orogenic collapse, extrusion processes, slab retreat, and channel flow (Platt, 1987; Dewey, 1988; Chemenda et al., 1995; Faccenna et al., 2001; Beaumont et al., 2004). As a contribution to this debate, we document the late tectonic evolution in the accretionary wedge of the western Alps, where final exhumation occurred while an extensional regime prevailed in the internal zones. In this classical example of a collision mountain range (e.g., Coward and Dietrich, 1989), the importance of widespread late extension in the internal zones was only recently discovered (see Selverstone, 2005, for review).

Major isolated ductile normal faults were first reported along the Queyras transect (Ballèvre et al., 1990; Blake and Jayko, 1990). Active extension was recognized by the current horizontal movements and seismicity (Sue et al., 1999, 2000) and has been interpreted as the continuation of the same long-lived extension at the scale of the internal arc (Sue and Tricart, 2003). It is associated with a dense network of "late Alpine" brittle normal faults (Tricart et al., 2004). Two possible driving mechanisms for this extension have been proposed in the inner western Alps: upward indentation of the European crust by the Apulian mantle (Lardeaux et al., 2006) or gravitational collapse of the overthickened European crust (Sue et al., 2007). To provide new constraints on this issue, we investigated a key zone of the Alpine internal arc.

We focus here on the Schistes lustrés of eastern Queyras, where various outcrops in meta-pelitic schists and meta-basalts display extensional structures developed at the ductile-to-brittle transition during final exhumation. Through microtectonic analysis, we characterize the tectonic regime that prevailed when the blueschist-bearing units cooled from greenschist facies to brittle conditions. The corresponding pressure-temperature-time (*P-T-t*) path is discussed on the basis of the available thermochronological

[†]E-mail: stephane.schwartz@ujf-grenoble.fr

data and new thermobarometric data from two generations of quartz-chlorite–filled veins. In light of our results, we propose a tectonic scenario to explain this regional extension.

GEOLOGICAL CONTEXT

Alpine evolution along the Eurasia-Africa boundary was initially dominated by plate divergence, which induced Mesozoic rifting and ocean opening. Since the Cretaceous, plate convergence has resulted in subduction and collision (Rosenbaum and Lister, 2005, and references therein). This study focuses on the core of the western Alpine arc, in the Queyras region and the surrounding valleys, close to the watershed (France-Italy border). Geologically, the area belongs to the Piedmont zone of the Alpine internal arc (Fig. 1). This internal arc consists of a pile of metamorphic nappes with dominant Paleogene north- or northwest- or west-directed structures. The Alpine external arc is less shortened (Gratier et al., 1989) and only slightly metamorphosed, ranging up to greenschist-facies conditions (Goffé et al., 2004), and it was built mainly during the Neogene. This contrast between the arcs is explained by the existence of a west-directed major structure, the Penninic deep crustal thrust, along which the internal arc overrides the external arc (Tricart, 1984; Nicolas et al., 1990; Schmid and Kissling, 2000). This Oligocene thrust surface was reactivated as a detachment at the end of the Oligocene, while the "late Alpine" extensional tectonic regime developed in the Alpine internal arc (Tricart et al., 2001).

General Structure of the Alpine Internal Arc along the Queyras Transect

Along the Queyras transect, four main units (Fig. 2), originating from distinct paleogeographical domains, form the Alpine internal arc (Lemoine et al., 1986; Deville et al., 1992; Lardeaux et al., 2006).

The Briançonnais Zone

The Briançonnais zone derives from the European margin of the Tethys. It consists of mainly late Paleozoic to Mesozoic sediments and pre-Alpine basement rocks. A remarkable nappe stack involves pre-, syn-, and postrift Tethyan sediments originating from a stretched margin (e.g., Claudel and Dumont, 1999). This stack of cover nappes was shortened during the Oligocene, and, because it is mechanically a multilayer with mechanical contrast, it gave rise to regional west- and east-verging folds and associated thrusts. The latter are known as the Briançonnais back folds and back thrusts, which correspond

to the present-day Alpine fan-shaped structure (Tricart, 1984) metamorphosed under greenschist/blueschist-facies conditions (Goffé et al., 2004, and references therein). The Briançonnais zone was subsequently crosscut by a dense network of extensional-transtensional faults during the Neogene (Sue and Tricart, 2003). The onset of faulting remains poorly dated.

The Piedmont Schistes Lustrés Unit

The Piedmont Schistes lustrés unit originated in the distal European margin and from the nearby oceanic domain (Lemoine et al., 1986). Metamorphic marls, clays, and limestones dominate (calc-schists) and enclose hectometric to kilometric boudins of Triassic dolomites or Jurassic ophiolites (Tricart and Lemoine, 1986; Lagabrielle and Polino, 1988; Deville et al., 1992). Thrusting under blueschist-facies conditions during the Paleocene–early Eocene built an accretionary wedge that was strongly redeformed when collision relayed subduction in Paleogene time (Agard et al., 2002; Lardeaux et al., 2006; Tricart and Schwartz, 2006). Finally, the extensional structures described here were developed, which we can demonstrate to be mainly Neogene in age (Schwartz et al., 2007).

The Monviso Ophiolitic Unit

The Monviso ophiolitic unit contains major remnants of the Tethyan oceanic lithosphere that were strongly deformed and metamorphosed under eclogite-facies conditions (Lombardo et al., 1978; Schwartz et al., 2000; Rubatto and Hermann, 2001) during the Eocene (Duchêne et al., 1997). Contrasted eclogitic conditions (e.g., Schwartz et al., 2000) indicate that the Monviso massif is composed of imbricate units, rapidly exhumed (1 cm/yr) within the subduction channel during the Eocene and accreted beneath the Schistes lustrés unit under blueschist-facies conditions at 20–35 km depth (Schwartz et al., 2000, 2001). The Monviso eclogites are separated from the Dora-Maira massif by a ductile normal fault (Blake and Jayko, 1990; Philippot, 1990; Schwartz et al., 2001).

The Dora-Maira Crystalline Massif

The Dora-Maira crystalline massif derives from the European margin basement. The nappe pile is bent into a N-S–trending antiform, which gives the massif its gneissic dome structure. Imbricated tectonic slices with contrasting metamorphic rocks (orthogneisses, eclogitic metasediments, coesite-bearing quartzites) were subducted to varied depths, down to 120 km (Chopin et al., 1991; Compagnoni and Rolfo, 2003), and exhumed rapidly (3 cm/yr) during the Oligocene (e.g., Rubatto and Hermann, 2001). This fast exhumation stage led
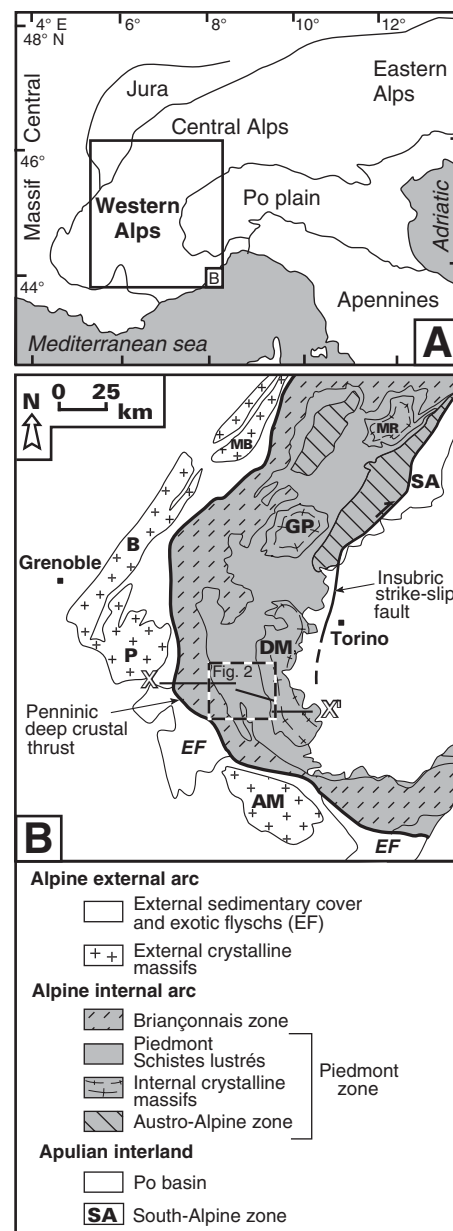
Figure 1. (A) Geographical setting of the western Alps showing location of (B). (B) Tectonic sketch map of the western Alps between France and Italy. The rectangle locates the studied area (Fig. 2). The Alpine internal arc is bounded by the Penninic deep crustal thrust to the west and by the Insubric fault to the east. External crystalline massifs: MB—Mont-Blanc, B—Belledonne, P—Pelvoux, AM—Argentera-Mercantour. Internal crystalline massifs: MR—Mont-Rose, GP—Gran-Paradiso, DM—Dora-Maira, SA—South Alpine zone. X-X′—trace of the cross sections presented in Figure 11.
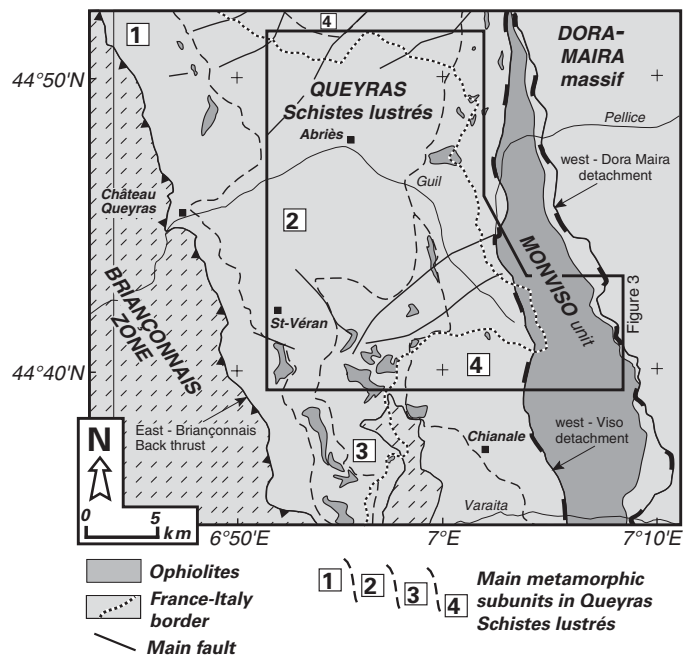
Figure 2. Simplified tectonic map of the studied area. The Schistes lustrés accretionary wedge encloses scattered meta-ophiolitic bodies. This wedge is bounded by two major faults: the east Briançonnais back-thrust fault (west-dipping reverse fault) and the west Monviso detachment (west-dipping ductile normal fault). The four metamorphic subunits comprising the Schistes lustrés unit are delimited (Tricart and Schwartz, 2006). The polygon locates the map in Figure 3.

and was developed at the blueschist-greenschist facies transition. The initial fold axes strike W-E to WSW-ENE and are also trended transverse to the belt direction. They are generally oblique by only 20°–30° to the previous one. These folds are south verging, and superimposition on the oldest folds results in nice refolded hinges roughly sharing the same axis. In the present structure, these folds trend close to W-E at the regional scale. The latest folds were developed under greenschist-facies conditions and trend N-S, turning progressively toward NNW-SSE further toward the south. They are east-directed isoclinal folds that display a 30°–60° west-dipping axial surface. Variable, often intense stretching close to E-W direction, i.e., transverse to the belt, has produced curved hinges or even sheath folds at the outcrop scale. Where fold hinges are absent, superimposed deformation has resulted in an omnipresent planar and linear (S + L) structure parallel with the monoclinal bedding. The planar structure results from transposition of the older schistosities, now parallel with the latest west-dipping schistosity (Fig. 3A). This composite schistosity bears a strong west-plunging stretching lineation (Fig. 3A) that generally corresponds to the primitive stretching lineation (glaucophane) transposed onto the latest one underlined by albite, chlorite, or actinolite. Presently, west-dipping (or SW-dipping) bedding and schistosity surfaces in Queyras Schistes lustrés (Fig. 3A) parallel the Monviso and Dora-Maira nappe stack.

Metamorphic Evolution of the Schistes Lustrés Unit

As previously discussed, four subunits (Fig. 2) have been identified in the Schistes lustrés unit. All of them have undergone typical blueschist-facies pressure-temperature (*P-T*) conditions (Caron, 1979; Pognante and Kienast, 1987; Caby, 1996). In detail (Rolland et al., 2000; Agard et al., 2001; Tricart and Schwartz, 2006), these conditions increase eastward from low-temperature blueschist conditions (see Fig. 3B) in the western Queyras (subunit 1: >9 kbar, 300 °C) up to the conditions of the blueschist-eclogite transition in eastern Queyras (unit 4: >13 kbar, >450 °C). In the easternmost domain, in the footwall of the west Monviso ductile normal fault, all metamorphic assemblages are eclogitic (Figs. 3A and 3B). Everywhere in the Schistes lustrés unit, the retrograde metamorphism stages have remained in the field of the chlorite-actinote-albite paragenesis (Fig. 3B), with no temperature increase (Tricart and Schwartz, 2006). The *P-T* paths display clockwise loop geometries, keeping a record of

rocks of the Dora-Maira to be accreted beneath the Schistes lustrés–Monviso units under blueschist-facies conditions.

General Ductile Structure of the Schistes Lustrés Unit in Queyras

The structure of the Schistes lustrés unit in Queyras and the surrounding valleys has been clarified by systematic mapping (Lagabrielle and Polino, 1988; Deville et al., 1992; Tricart et al., 2003) and detailed petrological studies (Agard et al., 2001; Tricart and Schwartz, 2006).

At a regional scale, the initial structure has been reconstructed as a pile of thrust sheets associated with the development of blueschist schistosity parallel with bedding. Each thrust sheet has a primitive lateral extension of at least several tens of kilometers, and each contains a single sedimentary series only a few hundred meters thick, detached along Triassic evaporites (distal margin series) or along serpentinite-derived sedimentary breccias (oceanic series). In the present structure, remnants of these décollement levels parallel the general bedding and schistosity, have a thickness often reduced

to a few meters or less, and contain boudins of Triassic dolostones or varied ophiolites (Tricart and Lemoine, 1986).

Contrasting high-pressure–low-temperature metamorphic initial conditions in this nappe pile allow four subunits to be recognized, called 1–4 in Figures 2 and 3. This early stack is interpreted as an accretionary wedge (Schwartz, 2000; Tricart and Schwartz, 2006), as already proposed from structural observations farther north in the same Piedmont zone (Deville et al., 1992; Agard et al., 2001; Ganne et al., 2005).

Detailed structural analysis shows that the initial nappe stack has been deformed by three successive generations of folds (Caron, 1979; Tricart and Schwartz, 2006). The oldest folds initially developed as north-directed recumbent folds, developed under blueschist-facies conditions, with a W-E to WNW-ESE axial direction. A strong associated stretching lineation was oriented parallel with this axial direction. These folds presently still trend close to W-E at the regional scale, and their limbs, in spite of subsequent refolding, can be followed up to several tens of kilometers. The second generation of folds also consists of recumbent folds

the early prograde evolution (Fig. 3B). These paths are regionally coherent in all subunits (Tricart and Schwartz, 2006), including their northern extension in the Cottian Alps (Agard et al., 2001). These metamorphic subunits have been the subject of Ar-Ar geochronological studies (Agard et al., 2002), and the ages of high-pressure metamorphism range between 62 and 55 Ma.

FROM DUCTILE TO BRITTLE DEFORMATION: THE FAULTED BOUDINS

From place to place within the pile of metamorphosed marly and calcareous formations that compose the Queyras Schistes lustrés, inserted interbedded relatively thin beds with a peculiar lithology favor boudinage. They are mainly (1) up to 2–3-m-thick basaltic flows or basalt-derived sands ("prasinites") and (2) up to a 0.2–0.3-m-thick meta-arkosic sands with continent-derived clasts. The selected outcrops (e.g., Figs. 4, 5, and 6) are relatively easy to reach along the watershed, around the Col Agnel (2746 m), which is a pass between France and Italy that is suitable for motor vehicles.

Postfolding Boudinage and the Onset of Regional-Scale Extension

Isolated beds of prasinite or meta-arkose within alternating metamorphosed pelagic marls (calc-schists), clay-rich limestones (micaceous marbles), or siliceous limestones (banded marbles) display boudin structures. They are essentially symmetrical boudins that have veins normal to the bedding and to the main composite schistosity. According to the lithology and using the nomenclature of Goscombe et al. (2004), unmodified geometries vary between two end members: drawn boudins (rare) and torn boudins (dominant). Phengite-rich arkose beds display a tendency to multiple-layer boudinage (Fig. 4). From place to place, boudinage becomes asymmetrical due to some slip along the interboudin surface. Slip sense is synthetic in a general top-to-the-east shear along bedding. In a few localities, this shearing is accentuated, resulting in shear-band boudins (Goscombe et al., 2003). This local evolution has not been taken into account here.

Boudinage postdates the last generation of folds, since their limbs and hinges are everywhere affected. In the boudin necks, veins are filled with quartz fibers, albite, and chlorite (Fig. 4A); they correspond to the so-called "Alpine veins" in Alpine classical literature (Tricart et al., 2003). In the veins that escaped subsequent deformation and still contain quartz
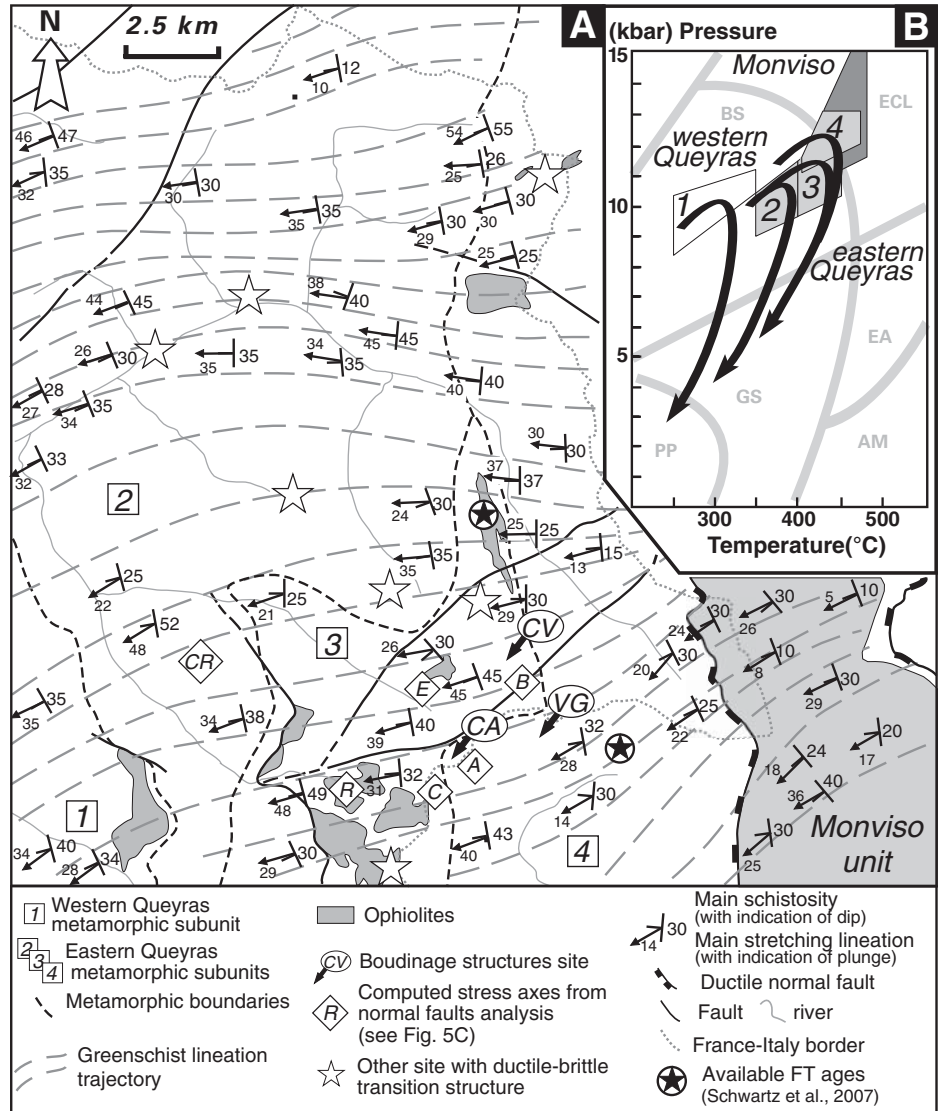

Figure 3. (A) Structural map of the Schistes lustrés unit. The main schistosity corresponds to the early blueschist schistosity reactivated or transposed into greenschist-facies conditions. The main stretching lineation corresponds to the latest direction of stretching in greenschist-facies conditions along which earlier stretching mineral lineation (high-pressure phengite, glaucophane) are parallelized. Localization of analyzed sites for boudinage structures: CV—Col Vieux, VG—Vallone del Giarus, CA—Caramantran. Localization of sites where a paleostress tensor was computed: B—Brèche de Ruine, C—Chamoussière, E—Eychassier, R—Roche Ronde, A—Col Agnel, CR—Château Renard (see plot in Fig. 5C and Table 1 for details). (B) Blueschist pressure-temperature (*P-T*) conditions in the Queyras Schistes lustrés (modified after Tricart and Schwartz, 2006). The eclogitic conditions in the Monviso ophiolitic unit are included for comparison (Schwartz et al., 2000). Metamorphic facies are from Spear (1993): GS—greenschist, BS—blueschist, EA—eclogite, ECL—epidote amphibolite, AM—amphibolite. FT—fission track.

fibers with nondistorted crystal lattice (Durney and Ramsay, 1973), it appears that these fibers grew subperpendicular to the vein planes during a coaxial opening (Fig. 4C). We thus interpret them as syntectonic fibers (fiber I) in response to coaxial extension, the stretching axis lying within the bedding. Within the Schistes lustrés pile, this boudinage is restricted to very few lithologies and represents the first expression of a brittle extension, while the coeval ductile extension within the other lithologies represents the ultimate ductile deformation (Fig. 5). Such a
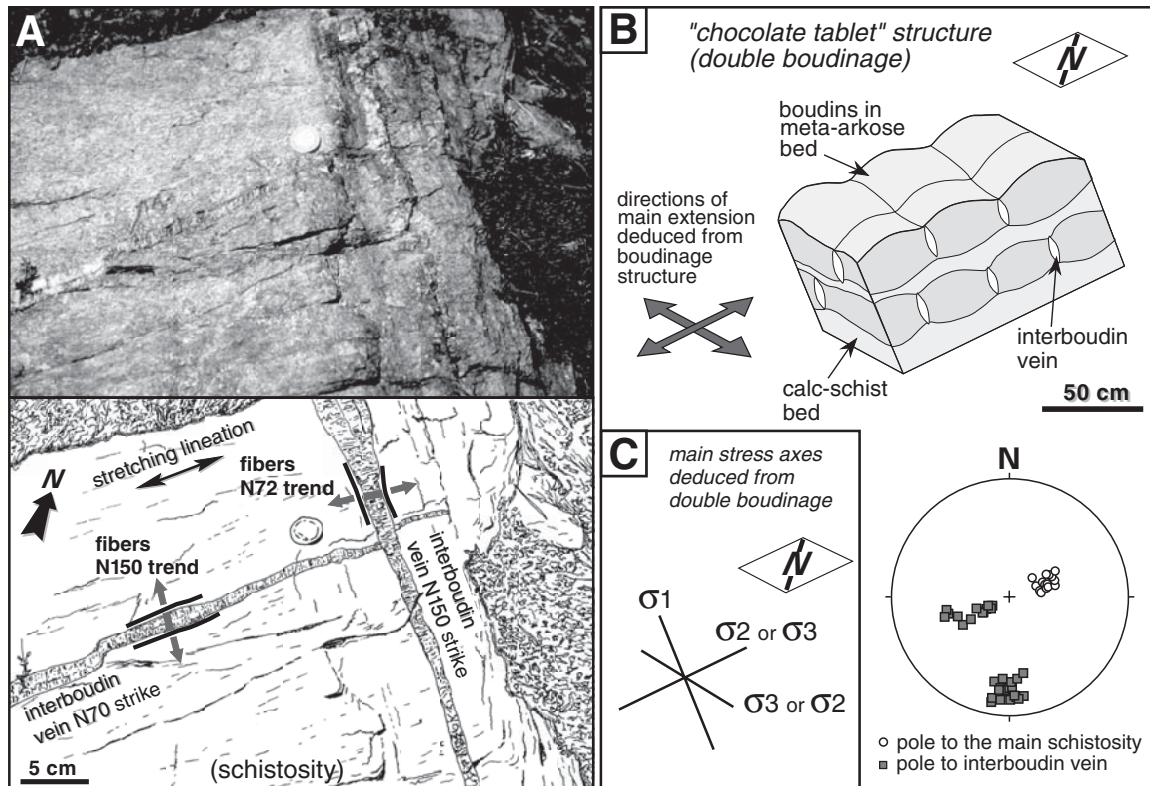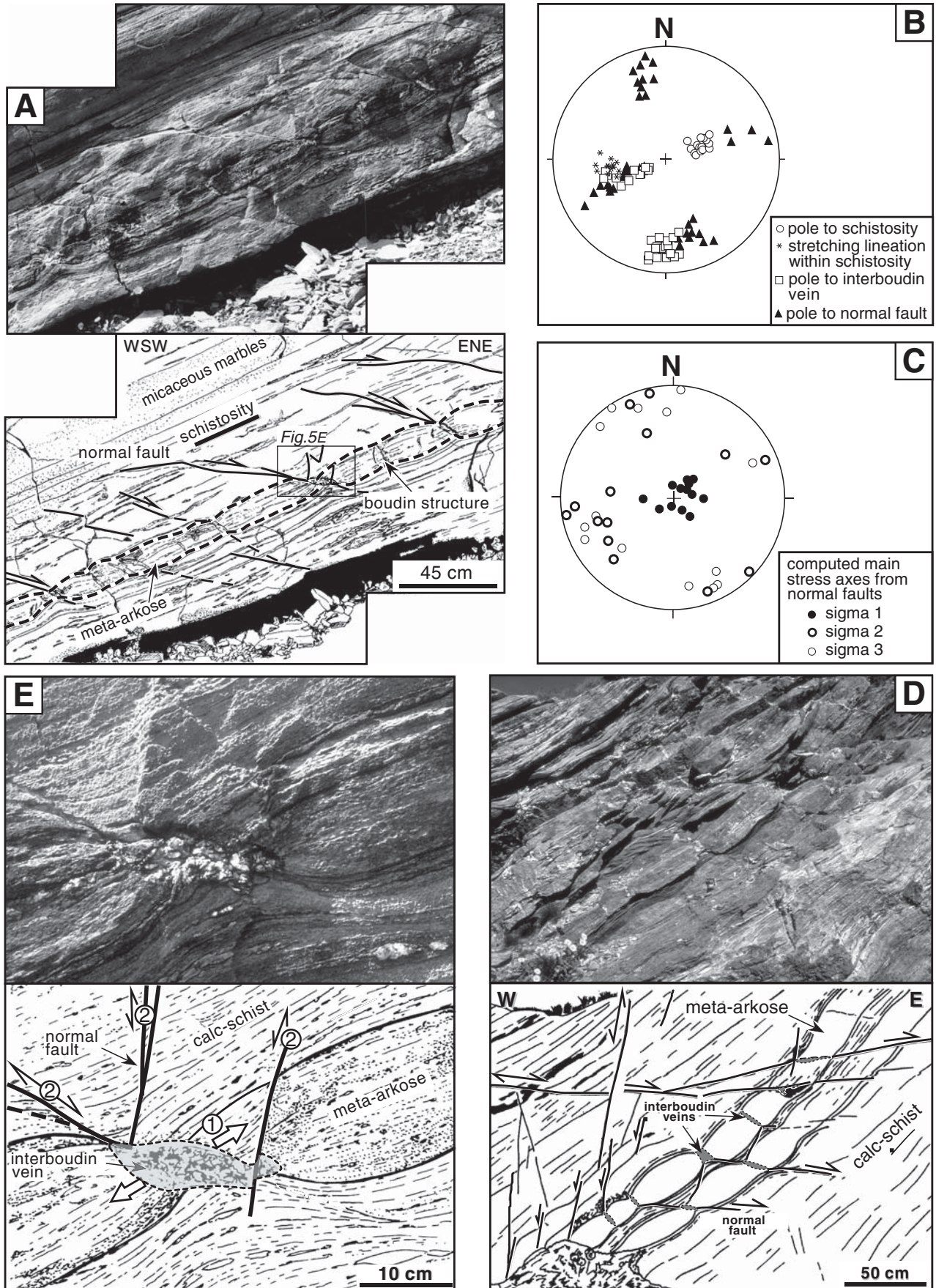
Figure 4. Double boudinage developed at the ductile-brittle transition in meta-arkoses imbedded in calc-schists and marbles at site CV. (A) Photograph and interpretation of a WSW gently dipping meta-arkose bed showing the main schistosity parallel to the bedding, and bearing the main stretching lineation (same structures as in Fig. 3). As the result of double boudinage, the bedding is crosscut by two near-vertical quartz-chlorite-albite veins. The vein with ENE-WSW (N70°) strike is crosscut by the vein with NNW-SSE (N150°) strike. Quartz fibers in veins with N150 and N72 trend, respectively, remain nearly perpendicular to vein planes: we interpret them as syntectonic fiber I, later poorly deformed. Boudinage resulting from stretching along a NNW-SSE direction was followed by another boudinage in response to ENE-WSW stretching, but in nearby outcrops, the reverse chronology may be observed. This suggests that at the regional scale, a single double boudinage deformation event occurred. (B) Interpreted structures sketched in block diagram and plotted on a Wulff net, lower-hemisphere projection. Double boudinage of the brittle meta-arkose beds within ductile calc-schists result in "chocolate tablet" structure development. (C) The proposed corresponding main stress axes. The σ3 axis and σ2 axis (with a stress magnitude σ2 ≈ σ3) are normal to the veins; σ1 axis is normal to the boudinaged bed, where σ1 > σ2 ≈ σ3 suggests a prolate, almost uniaxial stress ellipsoid.

Figure 5. Ductile stretching–boudinage–normal faulting sequence in alternating marbles, calc-schists, and meta-arkoses. (A) At VG site, the gently west-dipping metasedimentary pile (circle in stereoplot B) contains a close to W-E stretching lineation (star in stereoplot B) developed under greenschist-facies conditions (see Fig. 3 for regional-scale trajectory). Boudinage of isolated meta-arkose beds (interboudin veins: square in stereoplot B) occurred while marbles and calc-schists achieved their ductile stretching. Subsequently, small-scale normal faults (triangles in stereoplot B) crosscut the whole pile. This ductile-to-brittle sequence of deformation occurred during the synextensional final exhumation and cooling of the structure. (B) Attitude of the microstructures represented in part A plotted on a Wulff net (lower-hemisphere projection). Passing from ductile to brittle, stretching was accompanied by the development of a close to N-S extension in complement with nearly E-W extension. Two suborthogonal families of small-scale normal faults overprint the suborthogonal boudins (chocolate tablet structure: see Fig. 4). (C) Plot (same projection as in B) of the main stress axes computed from striated normal faults in sites localized in Figure 3 (see Table 1 for details). The direct inversion analytic method (Angelier, 1990) provides the attitude of the main stress axes. The σ1 axes are grouped near the center of the diagram, while the σ2 and σ3 axes are scattered at its periphery, partly due to permutation of σ2 and σ3 axes from one site to another. This illustrates a multitiered, almost radial brittle extension, consistent with the low mean value (0.34) computed for the ratio of the principal stress difference (σ2 – σ3/σ1 – σ3). The steep plunging σ1 axes toward the east are explained by the progressive westward tilting of the structure during normal faulting. (D) Other example of normal faults overprinting the boudins at CV site. (E) Detail of A showing an interboudin vein affected by small-scale normal faulting. The faults appear to have nucleated along the interboudin veins. 1 and 2 refer to boudinage stage and to the subsequent normal faulting stage, respectively.

WSW

micaceous marbles

schistosity

normal fault

Fig.5E

boudin structure

meta-arkose

ENE

45 cm

A

B

N

○ pole to schistosity
✳ stretching lineation within schistosity
□ pole to interboudin vein
▲ pole to normal fault

C

N

computed main stress axes from normal faults
● sigma 1
◉ sigma 2
○ sigma 3

E

normal fault

calc-schist

meta-arkose

interboudin vein

10 cm

D

W

meta-arkose

interboudin veins
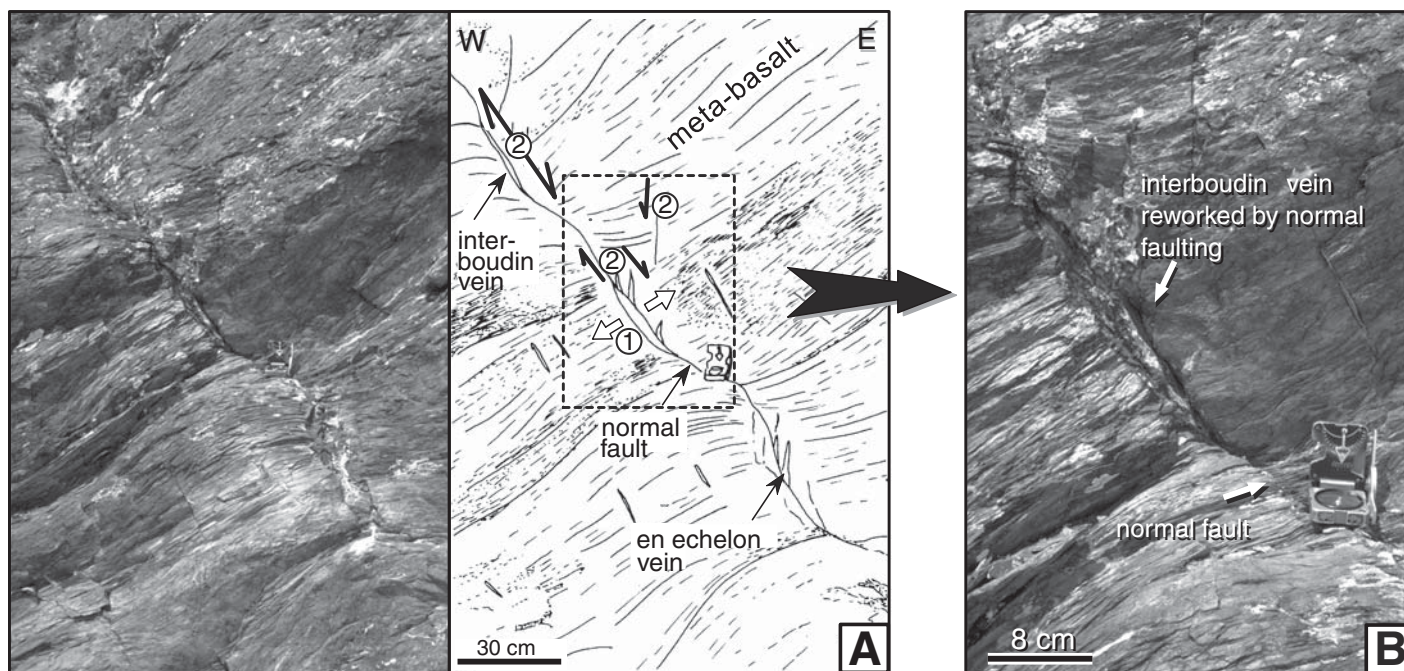
normal fault

calc-schist

E

50 cm

Figure 6. Normal faulting of boudins in schistosed meta-basalts at CA site. Two generations of veins filled with syntectonic quartz-albite-chlorite fibers may be distinguished: (1) interboudin veins normal to the bedding (fiber I) and (2) en echelon veins along the normal faults (fiber II). Some interboudin veins remain preserved, while others are variably sheared. (A) General view. (B) Detail.

boudin development illustrates how the Schistes lustrés evolved from ductile to brittle deformation conditions. An important conclusion is that, subsequent to the folding and thrusting history described in "General ductile structure of the Schistes Lustreés Unit in Queyras" the regional-scale regime of deformation has clearly become extensional.

Chocolate Tablet Boudinage as the Result of Multitiered Extension

In the entire Queyras area, the boudinage described in "Post-folding boudinage and the onset of regional scale extension" occurred along two directions, resulting in two sets of veins oriented normal or at high angle to the bedding (Fig. 4B). Veins with NNW-SSE strike result from ENE-WSW stretching within the beds. Veins with ENE-WSW strike result from NNW-SSE stretching. Both axes of stretching are parallel with the bedding. Locally, the NNW-SSE vein set becomes oblique to the bedding, suggesting asymmetric boudinage (Fig. 5A). Crosscutting relationships between the two sets of boudins does not allow establishment of a simple chronology. In some places, one boudin set is overprinted by the other, whereas in other places, the reverse situation is observed. We thus conclude that both sets are globally coeval and represent a chocolate tablet or double-boudinage structure (Ramsay, 1967). This implies a multitiered extension within the bedding accommodating a compression normal to the bedding.

Small-Scale Normal Faulting and the Generalization of Brittle Extension

From the interboudin veins, extensional faults developed at the centimeter- to meter-scale (Fig. 5). These faults are either isolated or grouped as pairs of conjugate faults. Normal sense of faulting is constrained by offset of faulted beds, frequently associated with drag folding. Normal faulting is not restricted to the sites that display earlier boudinage but may be observed everywhere in the Queyras unit, whatever the lithologies. This illustrates that the entire Queyras structure became fully brittle as extension continued. Along these normal faults, arrays of en echelon veins also developed, often with a sigmoid geometry (Fig. 6). They contain syntectonic fibers of quartz and greenschist-facies mineral such as albite and chlorite, which represent fiber II in the following sections. Where normal faults intersect the veins in the boudin necks, the chronology between fiber I (synboudinage) and fiber II (subsequent faulting) may be clearly established. This dense, small-scale normal faulting with centimeter-scale throw was followed by the development of more widely spaced major normal faults (usually kilometer-sized or more) with increased throw (usually several meters to several tens of meters). This corresponds to the classical localization of a primitive, more distributed brittle extension (e.g., Sue and Tricart, 2003). It resulted in the regional-scale normal faulting that is widespread today in the entire Queyras Schistes lustrés unit, and also in the entire Briançonnais and Piedmont zones. This normal fault array remains active, explaining the ongoing earthquake activity down to 10–15 km depth (Sue and Tricart, 2003).

Normal Faulting Confirms the Multitiered Character of Late Alpine Extension

A remarkable feature concerning small-scale normal faulting is that the faults seem to have nucleated within the boudin necks and propagated upward and/or downward into the calc-schists and marble beds that escaped boudinage. The direction of brittle extension deduced from the orientation of small-scale normal faults, notably the conjugated ones, parallels the direction of stretching associated with boudinage. This suggests the continuity of the same tectonic regime as normal faulting became the main process of deformation when the whole Schistes lustrés structure entered into the brittle domain. This observation is true for both sets of boudins described in "Chocolate tablet

boudinage as the result of multitiered extension," and small-scale normal faults developed along two main directions: NNW-SSE and ENE-WSW. Crosscutting relationships suggest to us that both sets are coeval and formed in response to the same multitiered extensional regime. This regime persisted when major faults developed, also along the same two directions. In most sites, measurement of striated faults allowed us to compute a reduced stress tensor (Table 1; Fig. 5C), which confirms that the tectonic regime associated with normal faulting is a multitiered, almost radial, extension (Tricart et al., 2004). The amount of extension along the principal stress axes $\sigma2$ and $\sigma3$ is comparable from one site to another. These axes frequently exchanged with each other, one of which was oriented NNW-SSE and the other ENE-WSW (Fig. 4C). The computed stress axis $\sigma1$, along which the major shortening occurred, remained oriented subvertical.

FROM DUCTILE TO BRITTLE EXTENSION: *P-T* ESTIMATES

This analysis focuses on the two generations of fibers related to the boudinage and to the subsequent normal faulting of the boudinaged structures, described in "From ductile to brittle deformation: The faulted boudins." A fluid inclusion study of the quartz fibers provided their probable *P-T* conditions of formation, while the composition of the associated chlorites allowed us to make independent temperature estimates. Zircon fission-track data (Schwartz et al., 2007) provide a time calibration that complements these new data.

TABLE 1. COMPUTED MAIN STRESS AXES FROM NORMAL FAULTS PLOTTED IN FIGURE 5C

Stress axes	Azimuth (°)	Plunge (°)	Site	Longitude	Latitude	Lithology
$\sigma1$	149	73	Brèche de Ruine	06°59′54.34″E	44°41′53.01″N	Calc-schist
$\sigma2$	264	7				
$\sigma3$	356	15				
$\sigma1$	62	75	Chamoussière 1	06°57′30.60″E	44°40′51.16″N	Calc-schist
$\sigma2$	223	14				
$\sigma3$	314	5				
$\sigma1$	229	71	Chamoussière 2	06°57′30.60″E	44°40′51.16″N	Calc-schist
$\sigma2$	335	5				
$\sigma3$	67	14				
$\sigma1$	56	71	Eychassier 1	06°58′17.27″E	44°42′03.13″N	Calc-schist
$\sigma2$	235	19				
$\sigma3$	325	0				
$\sigma1$	85	71	Eychassier 2	06°58′17.27″E	44°42′03.13″N	Calc-schist
$\sigma2$	347	3				
$\sigma3$	256	18				
$\sigma1$	49	64	Roche Ronde 1	06°56′30.33″E	44°40′38.08″N	Meta-basalt
$\sigma2$	248	25				
$\sigma3$	154	7				
$\sigma1$	43	79	Roche Ronde 2	06°56′30.33″E	44°40′38.08″N	Meta-basalt
$\sigma2$	160	5				
$\sigma3$	251	10				
$\sigma1$	264	59	Roche Ronde 3	06°56′30.33″E	44°40′38.08″N	Meta-basalt
$\sigma2$	52	28				
$\sigma3$	150	14				
$\sigma1$	351	79	Roche Ronde 4	06°56′30.33″E	44°40′38.08″N	Meta-basalt
$\sigma2$	260	0				
$\sigma3$	170	11				
$\sigma1$	141	63	Roche Ronde 5	06°56′30.33″E	44°40′38.08″N	Meta-basalt
$\sigma2$	338	27				
$\sigma3$	244	7				
$\sigma1$	53	70	Col Agnel 1	06°58′46.64″E	44°41′02.35″N	Marble
$\sigma2$	251	19				
$\sigma3$	156	6				
$\sigma1$	42	67	Col Agnel 2	06°58′46.64″E	44°41′02.35″N	Marble
$\sigma2$	135	1				
$\sigma3$	225	23				
$\sigma1$	193	79	Château Renard 1	06°54′26.78″E	44°41′53.16″N	Marble
$\sigma2$	69	6				
$\sigma3$	338	9				
$\sigma1$	94	59	Château Renard 2	06°54′26.78″E	44°41′53.16″N	Marble
$\sigma2$	274	31				
$\sigma3$	4	0				

Note: For each main stress axis, azimuth and plunge values are given. Measurement sites regroup along or near the French-Italian water divide, corresponding to the main Alpine crest line (see location in Fig. 3).

Microthermometry Contribution

The sampled outcrops clearly display the sequence of deformation starting in greenschist-facies conditions (see section "From ductile to brittle deformation: The faulted boudins"): (1) fully ductile extension, (2) semibrittle extension with boudin development, and (3) fully brittle extension with normal faulting, occurring first at a small-scale, and then affecting the whole regional-scale structure. The three sites illustrated here—Vallon Giarus, Col Vieux, Caramantran—belong to metamorphic units 3 and 4 (location in Fig. 3A). Two generations of syntectonic quartz fibers, associated with chlorite and albite, were analyzed: fiber I, within interboudin veins, developed during semibrittle extension (stage 2) and fiber II, along micronormal faults, developed later (beginning of stage 3). Microthermometric study was performed with a Linkam THMSG 600 on double-polished, 150-µm-thick thin sections subjected to

heating-freezing cycles (Shepherd et al., 1985). In the case of two-phase inclusions, two temperatures were measured during each cycle: the melting temperature of ice (*T*m ice) and the homogenization temperature (*T*h). *T*m ice, corresponding to the melting of the last ice crystal in the inclusion, is a function of the dissolved salt concentration in the fluid phase. *T*h corresponds to the disappearance of the vapor bubble in the inclusion, when the fluid trapped in this inclusion becomes homogeneous. The eutectic melting temperature, generally used to characterize the nature of the dissolved species, could not be accurately determined. Temperature measurements were reproducible within 0.2 °C for *T*m ice and within 0.5–1 °C for *T*h (Shepherd et al., 1985; Belkin, 1994).

More than 80 fluid inclusions were analyzed (Table 2). All inclusions were aqueous. Ice melting started at temperatures close to that of the NaCl-H_2O system eutectic, i.e., around −21 °C (Roedder, 1984; Crawford and Hollister, 1986).

The fluids were not pure dissolved NaCl. Salt content (in NaCl wt% eq.) was determined using the *T*m ice data, either graphically with the NaCl-H2O system phase diagram (Roedder, 1984) or analytically (Belkin, 1994). The NaCl contents were homogeneous and relatively weak, ranging between 0.5 and 7.3 wt% eq. NaCl. Comparable results have been obtained by Agard et al. (2000) in the northern extension of the Queyras Schistes lustrés (Cottian Alps), for greenschist retrograde fluids in metapelites. Our main result is that fluid compositions (fluid inclusion populations) differ in quartz fibers I and II. Such differences clearly support the chronological distinctions previously established between the different generations of veins.

Fiber I in Interboudin Veins

To avoid the remobilization of fluids after vein formation and the reequilibration of fluid inclusions in lower *P-T* conditions during subsequent system opening, fiber I samples were chosen

TABLE 2. FLUID INCLUSION DATA FROM VALLON GIARUS, COL VIEUX, AND CARAMANTRAN VEIN QUARTZ

Sample	N	T_m ice (°C)	T_h L-V (°C)	NaCl (wt% eq.)	Density (g/cm³)	Sample	N	T_m ice (°C)	T_h L-V (°C)	NaCl (wt% eq.)	Density (g/cm³)	Sample	N	T_m ice (°C)	T_h L-V (°C)	NaCl (wt% eq.)	Density (g/cm³)
VALLON GIARUS						CV16	17	−1.8	148.1	2.96	0.94	*CARAMANTRAN*					
VGO5	1	−3.1	161.8	5.01	0.94	CV16	18	−2.2	145.7	3.60	0.95	CA18	1	−1.6	160.5	2.63	0.93
VGO5	2	−2.3	157.4	3.76	0.94	CV16	19	−3.8	163.3	8.08	0.95	CA18	2	−1.6	158.0	2.63	0.93
VGO5	3	−2.3	165.5	3.76	0.93	CV16	20	−2.3	158.8	3.76	0.94	CA18	3	−1.6	166.1	2.63	0.92
VGO5	4	−2.3	159.7	3.76	0.94	CV16	21	−1.4	146.8	2.31	0.94	CA18	4	−1.6	230.4	2.63	0.85
VGO5	5	−2.3	157.3	3.76	0.94	CV16	22	−1.3	142.6	2.14	0.94	CA18	5	−1.2	137.6	1.98	0.94
VGO5	6	−2.3	161.8	3.76	0.94	CV16	23	−1.4	155.7	2.31	0.93	CA18	6	−0.7	233.0	1.16	0.83
VGO5	7	−1.5	155.2	2.47	0.93	CV16	24	−2.0	157.2	3.28	0.94	CA18	7	−0.9	234.0	1.49	0.83
VGO5	8	−1.8	161.9	2.96	0.93	CV16	25	−1.6	157.6	2.83	0.93	CA18	8	−0.9	233.3	1.49	0.83
VGO5	9	−1.7	154.7	2.79	0.94	CV16	26	−1.3	157.7	2.14	0.93	CA18	9	−1.3	169.1	2.14	0.92
VGO5	10	−3.2	162.3	5.17	0.94	CV16	27	−3.1	126.0	5.01	0.97	CA20	10	−1.1	153.0	1.82	0.93
VGO5	11	−3.1	181.3	5.01	0.93	CV16	28	−2.0	141.2	3.28	0.95	CA20	11	−1.0	216.5	1.65	0.86
VGO5	12	−4.6	145.8	7.25	0.97	CV16	29	−2.1	165.1	3.44	0.93	CA20	12	−0.9	147.6	1.49	0.93
VGO5	13	−3.0	155.9	4.86	0.95	CV16	30	−0.4	138.5	0.66	0.94	CA20	13	−0.9	148.3	1.49	0.93
COL VIEUX						CV16	31	−0.6	148.9	0.99	0.93	CA20	14	−1.0	156.9	1.65	0.93
CV12	1	−2.0	175.0	3.28	0.92	CV16	32	−0.7	138.5	1.16	0.94	CA20	15	−0.8	148.9	1.32	0.93
CV12	2	−1.9	188.5	3.12	0.91	CV16	33	−0.6	140.5	0.99	0.94	CA20	16	−0.7	165.4	1.16	0.91
CV12	3	−2.2	162.2	3.60	0.93	CV16	34	−1.1	143.1	1.82	0.94	CA20	17	−1.0	239.5	1.65	0.82
CV12	4	−1.9	139.4	3.12	0.95	CV16	35	−1.3	138.3	2.14	0.94	CA20	18	−1.1	249.7	1.53	0.86
CV12	5	−2.2	185.3	3.60	0.91	CV16	36	−2.3	142.3	3.76	0.95	CA20	19	−1.1	222.1	1.82	0.85
CV12	6	−1.7	141.0	2.79	0.95	CV16	37	−0.4	138.5	0.66	0.93	CA20	20	−1.2	210.9	1.98	0.87
CV12	7	−2.1	188.3	3.44	0.91	CV16	38	−1.7	173.5	2.79	0.92	CA20	21	−1.1	248.4	1.82	0.81
CV12	8	−3.7	172.4	5.93	0.94	CV16	39	−1.4	137.0	2.31	0.95	CA20	22	−0.7	147.2	1.16	0.93
CV12	9	−3.9	191.7	6.23	0.92	CV16	40	−2.2	168.5	3.60	0.93	CA20	23	−0.9	237.5	1.49	0.83
CV12	10	−3.1	170.6	5.01	0.94	CV16	41	−2.0	160.8	3.28	0.93						
CV12	11	−3.1	172.9	5.01	0.93	CV16	42	−2.1	126.8	3.44	0.96						
CV12	12	−2.8	175.0	4.55	0.93	CV16	43	−2.0	147.5	3.28	0.94						
CV12	13	−1.7	164.0	2.79	0.93	CV16	44	−2.1	162.4	3.44	0.93						
CV12	14	−2.3	162.8	3.76	0.93	CV16	45	−1.5	142.1	2.47	0.94						
CV12	15	−2.2	165.6	3.60	0.93	CV16	46	−1.9	170.0	3.12	0.92						
CV12	16	−2.0	169.3	3.28	0.93	CV16	47	−1.0	142.5	1.65	0.94						

Note: N—sample number; T_m ice—melting temperature; T_h L-V—homogenization temperature; NaCl (wt% eq.)—weight percent of NaCl.

carefully from interboudin veins that had not been subsequently sheared. Large-size (>20 μm in diameter) fluid inclusions were isolated within the quartz (Fig. 7A). In the T_h-T_m ice diagram, the fluids plot within a restricted field (Fig. 8A). T_h varied between 126.0 °C and 191.7 °C, with a mean value at 157.2 °C, whereas T_m ice varied between −4.6 °C and −0.4 °C, with a mean value at −2.1 °C. The T_m ice range allowed the nature of the fluids trapped in the inclusions to be characterized. They were biphase $NaCl$-H_2O fluids with chemical compositions ranging between 0.70 and 8.08 wt% NaCl eq. Using Zhang and Frantz's (1987) equations, microthermometric measurements (T_h vs. T_m ice) allowed us to determine the characteristic isochores for the synboudinage fluids.

Fiber II in Veins Associated with Normal Faults

The quartz fibers also contained fluid inclusions. In the T_h-T_m ice diagram, their physical parameters plot in a larger field (Fig. 8B). The prominent feature is the important variation of T_h, which ranges from 137.6 to 249.7 °C, versus T_m ice, which ranges from −1.6 to −0.7 °C (Table 2). Contrary to fiber I, two coexisting populations of fluid inclusions could be distinguished. A first population is similar to that observed in fiber I, with a large size (>20 μm in diameter) and an irregular shape, isolated within the quartz. For them, T_h was low, around 150 °C, and T_m ice ranged between −1.6 and −0.7 °C (Table 2). They are interpreted as primary inclusions trapped in syngreenschist minerals during early boudinage. The second population corresponds to fluid inclusions with a small elliptic shape, rarely more than 15 μm long (Fig. 7B). These inclusions are often stretched and coalescent within crystal growth planes, drawing linear "trails" of inclusions. For these "secondary" fluid inclusions, T_h ranges between 210.9 and 249.7 °C (Fig. 8B), whereas T_m ice is restricted to between −1.6 and −0.7 °C, with a mean value at −1.1 °C. The trapped fluids are homogeneous biphase $NaCl$-H_2O fluids. They contain moderate concentrations of salt, between 1.49 and 2.63 wt% NaCl eq., with an average composition around 1.70 wt% NaCl eq. The T_h variations toward the high temperatures (>200 °C) correspond to the reequilibration of the primary fluid inclusions at shallower depth during exhumation. The newly formed normal faults drained and partly remobilized the greenschist-facies fluids, including fluids trapped within inclusions, in the interboudin veins. Contrary to the
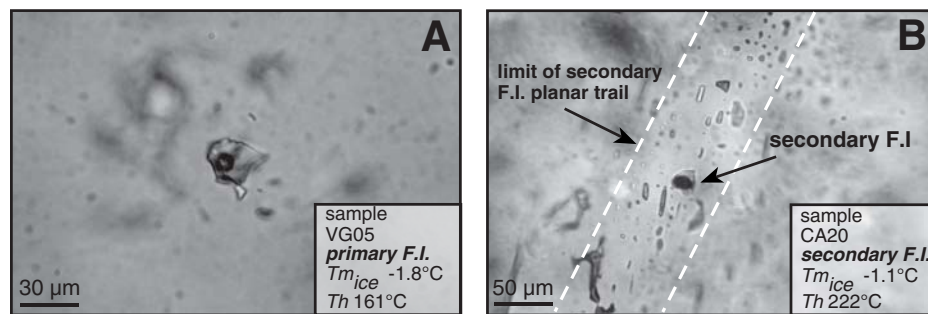

Figure 7. Photomicrographs of fluid inclusion (F.I.) populations in the two generations of fibers. (A) In syntectonic fiber I associated with boudinage, the primary fluid inclusions have a large diameter (>20 μm). (B) In syntectonic fiber II, associated with postboudinage micronormal faulting, the fluid inclusions have smaller diameters. The physical parameters of inclusions are indicated (see text for discussion).
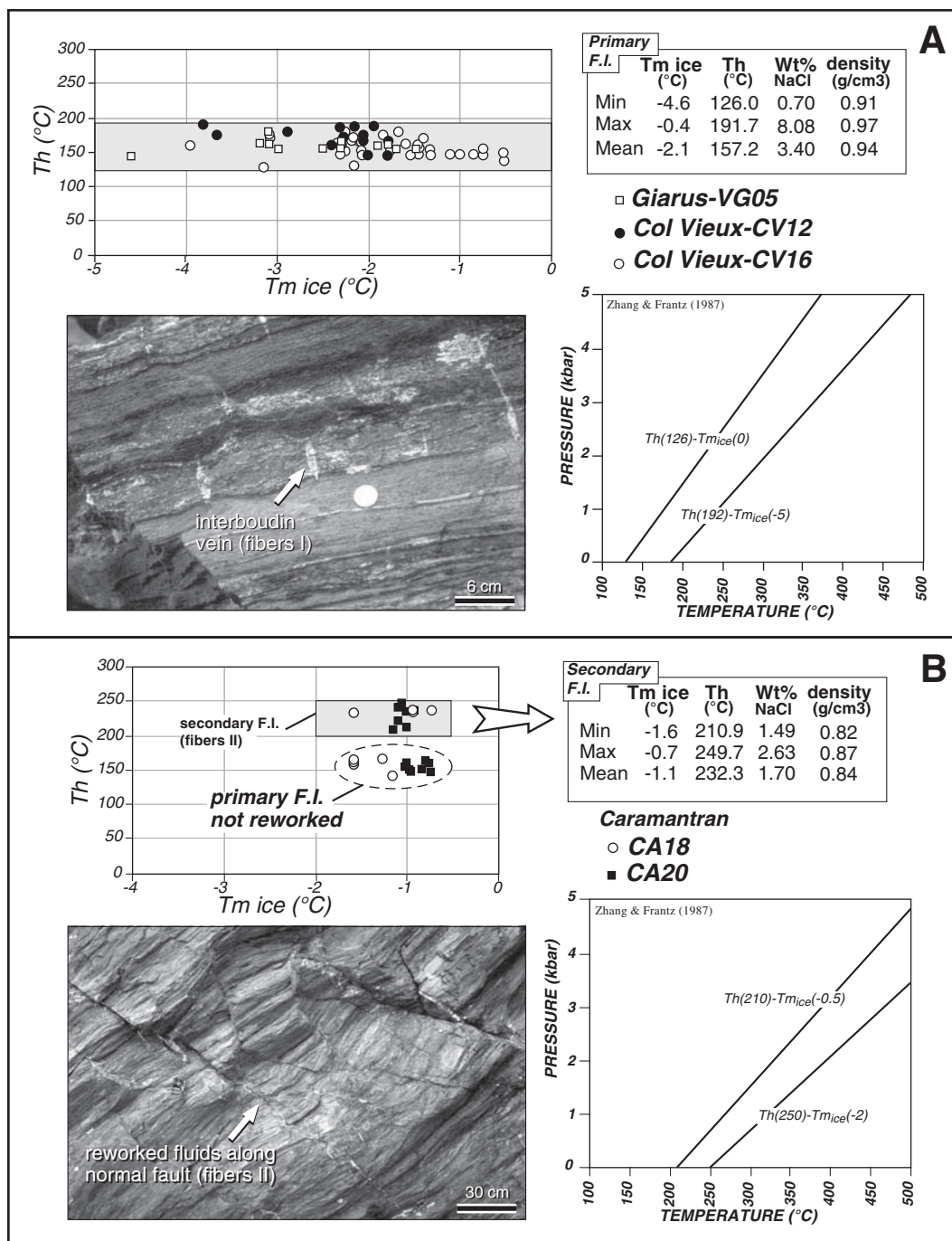
Figure 8. Physical parameters of fluid inclusions (F.I.) in interboudin veins and normal faults. The data are presented on Th vs. a Tm ice diagram and P-T isochores diagram. Only isochore limits are presented. (A) Fiber I shows fluid inclusions preserved from subsequent normal faulting. (B) Along early micronormal faults, two coexisting fluid inclusion populations are observed: unreworked primary inclusions inherited from the boudinage stage (fiber I) and secondary inclusions, reequilibrated during subsequent faulting (fiber II).

interboudin veins, the injected normal faults may have represented an open system, trapping fluids that reequilibrated with time. In this context, fluid inclusions with Th around 150 °C characterize the early interboudin veins. Shearing of interboudin veins along normal faults would have allowed the crystallization of new quartz fibers that equilibrated in lower-pressure conditions. In "secondary" inclusions, these minerals trapped fluids with higher Th, ar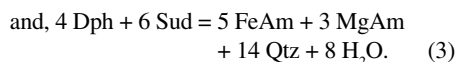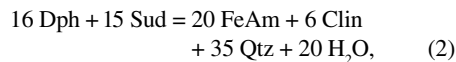ound 210–250 °C. Finally, from microthermometric parameters (Th and Tm ice), we deduced two limit isochores (Fig. 8B): Th (210)/Tm ice (−0.5) and Th (250)/Tm ice (−2). They correspond to the onset of brittle extension under greenschist-facies conditions.

Chlorite Composition as an Independent Thermometer

Limit values of the isochores associated with the two populations of fluid inclusions can be more precisely calibrated using an independent thermometer. Temperatures were calculated using the composition of chlorites as proposed by Vidal et al. (2001, 2006). The composition of chlorite is described with five end members: clinochlore (Clin), Fe- and Mg-amesite (FeAm and MgAm), daphnite (Daph), and Mg-sudoite (Sud), which are used to model the Fe-Mg, di-tri, and Tschermak chlorite substitutions. The solid-solution model between these end members is a site-mixing model that uses symmetric

Margules parameters and ideal intersite interactions. Chlorite crystallization temperatures were estimated from the location of three equilibria (two independents), which can be written for the chlorite-quartz-water assemblage observed in both generations of structures analyzed here:

$$2\ \text{Clin} + 3\ \text{Sud} = 4\ \text{MgAm} + 7\ \text{Qtz} + H_2O, \quad (1)$$

$$16\ \text{Dph} + 15\ \text{Sud} = 20\ \text{FeAm} + 6\ \text{Clin} \\ + 35\ \text{Qtz} + 20\ H_2O, \quad (2)$$

$$\text{and,}\ 4\ \text{Dph} + 6\ \text{Sud} = 5\ \text{FeAm} + 3\ \text{MgAm} \\ + 14\ \text{Qtz} + 8\ H_2O. \quad (3)$$

Temperatures were estimated assuming $H_2O = 1$. The presence of ferric iron in chlorite was estimated simultaneously using a criterion based on the convergence of equilibria of Equations 1–3 (Vidal et al., 2005, 2006). If necessary, the proportion of Fe^{3+} ($XFe^{3+} = Fe^{3+}/Fe$ total) was increased to a maximum value of 0.35 in 0.05 increments until convergence of Equations 1–3 within 25 °C. Composition, structural formula, and Fe^{3+} content of the analyzed chlorites are presented in Table 3. For chlorites in interboudin veins (fiber I), temperatures between 345 °C and 415 °C were calculated (Fig. 9A). On the other hand, chlorites in veins associated with normal faults (fiber II) provided lower temperatures, between 235 and 315 °C (Fig. 9A). The Fe^{3+} contents of chlorites were variable between the two generations of fibers. Chlorites in fiber I, equilibrated at higher temperatures, showed low XFe^{3+}, ranging from 0.10 to 0.25, while chlorites in fiber II, affected by normal faulting, showed higher XFe^{3+} (>0.30). These variations in XFe^{3+} are probably due to the percolation at low temperature of oxidizing meteoric fluids during normal faulting (Vidal et al., 2006). By coupling these data with the calculated isochores (Fig. 9B), we obtained a pressure range of 2.5–6 kbar (7.5–18 km) for the opening of the veins between the boudins (fiber I) and <1.7 kbar (<5 km) for the fibers in veins opened during the early normal faulting (fiber II).

DISCUSSION

P-T-t Evolution from Ductile to Brittle Extension

The *P-T* conditions proposed here concern the formation of the syngreenschist extensional structures at the ductile-to-brittle transition during the final exhumation of the Queyras (subunits 2, 3, and 4). This evolution postdates a blueschist-facies metamorphic history. Along the *P-T* path, boudinage (fiber I) occurred at 380 ± 35 °C and 6–2.5 kbar (Fig. 10). Incipient normal faulting (fiber II) took place subsequently at lower conditions, at 275 ± 40 °C and less than 1.7 kbar (Fig. 10). The final cooling of the Schistes lustrés unit was recently constrained by fission-track thermochronology (see location on Fig. 3A) on zircon (ZFT) and apatite (AFT), performed mainly in meta-ophiolitic bodies but also in meta-arkose beds (Schwartz et al., 2007). Indeed, the maximum temperature recorded by the fission-tracks method on zircons is 340 ± 40 °C. It corresponds to the upper limit of the partial annealing zone predicted from low- to zero-damage models (Brix et al., 2002; Rahn et al., 2004) and is in the range of the temperature estimated in fiber I. Since the AFT closure temperature is ~110 ± 10 °C (e.g., Reiners and Brandon, 2006), AFT ages give the maximum age for the crystallization of fiber II. Thus, the transition from ductile to brittle extension in the Schistes lustrés is given by the oldest ZFT age at ca. 27 Ma, whereas the minimum age of the brittle extension associated with the crystallization of fiber II is given by the youngest AFT age at ca. 10 Ma.

Interpreted Stress-Strain Evolution

The Schistes lustrés unit, which was initially entirely ductile, became partly brittle, then entirely brittle while it underwent synexhumation decompression and cooling. The structures developed at the ductile-brittle transition illustrate the evolution of the stress conditions and the strain geometry during this exhumation; the tectonic regime remains extensional. Next, we describe this continuous evolution in terms of successive stages.

Chocolate Tablet Boudinage

The geometry of deformation implies that the maximum principal stress axis ($\sigma 1$) remains subvertical and that the $\sigma 2$ and $\sigma 3$ magnitudes are quite similar (Fig. 4C). Globally, the extension is multidirectional, almost radial. According to our new *P-T* estimates, we propose that this boudinage occurred at relatively high temperature (415–345 °C) in a 6–2.5 kbar pressure range.

Small-Scale Multitiered Normal Faulting

All beds become brittle and are faulted, allowing the stress regime to be computed by fault-striae analysis (see Tricart et al., 2004, for review). The geometry of deformation has not changed, corresponding to multitiered extension, with a subvertical main compression axis (Fig. 5C). Lowering of fluid pressure recorded by fiber II (*P* <1.7 kbar) could have resulted from fluid escape along the new fault network and/or less fluid supply by retrogressed reactions.

Multiscale Multitiered Normal Faulting

Numerous, widespread minor faults with small movements are relayed, as active structures, by fewer faults of larger size with greater throw. Brittle deformation is more and more localized, while extension increases at the regional scale. The computed stress regime remains unchanged, corresponding to multitiered subhorizontal extension. This late normal faulting has been systematically analyzed and appears to be common in both the Briançonnais unit and Piedmont zone (Sue and Tricart, 2003). In the Schistes lustrés unit, normal faults, decametric to kilometric in size, are gently dipping and often listric in the bulk mass of calc-schists, but they are steeper in dolomites and ophiolites. Close to dip-slip movements often accompany the initial rupture, but more oblique movements (or even strike-slip movements) may follow. Regionally, the fault network is organized around two dominant trends, longitudinal and transverse to the belt (mean trends: NNW-SSE and SW-NE to E-W), which have worked contemporaneously. These faulting directions are comparable to the centimeter-scale faulting directions observed in the interboudins. The faults and microfaults are everywhere closely associated, and we relate them to the same regional-scale extension. The inversion of data (striae, striated planes) collected on these faults led us to compute stress tensors with a subvertical $\sigma 1$ axis. Comparable magnitudes for $\sigma 2$ and $\sigma 3$ give a prolate form to the regional-scale mean stress ellipsoid. For the Schistes lustrés unit, the resulting multitiered horizontal extension may be globally described by a flattened strain ellipsoid (Sue and Tricart, 2003). We consider this stress regime to be the continuation of the regime that was responsible for (1) early double boudinage (chocolate tablet development), and then (2) micronormal faulting of the boudins, when the Schistes lustrés structure entered into the brittle domain. In addition, a seismotectonic survey led Sue et al. (1999) to propose that the network of longitudinal and transverse faults remains active, resulting in a current multitiered extension within the upper 10–15 km crust below the internal Alpine arc. This suggests that the tectonic regime has not fundamentally changed along the final exhumation path in brittle conditions.

The Schistes Lustrés Unit in Queyras: A Tilted Accretionary Wedge

The main result of our tectonic analysis coupled with *P-T* estimates is that the tectonic regime experienced by the Schistes lustrés unit has

TABLE 3. MICROPROBE ANALYSES OF CHLORITE MINERALS ASSOCIATED WITH QUARTZ FIBERS I AND II

Fiber I

Sample	VG05-102	VG05-105	VG05-109	VG05-110	VG05-114	VG05-115	VG05-117	CA20-20	CV12-27	CV12-28	CV12-33	CV12-34	CV16-90	CV16-92	CV16-88	CV16-93
SiO_2	25.30	26.12	26.20	24.94	25.44	25.19	25.59	25.09	25.32	25.79	25.15	24.62	25.80	25.49	24.76	24.95
Al_2O_3	22.81	22.34	23.21	21.29	21.89	23.18	21.02	21.11	22.52	19.93	23.18	22.07	21.03	21.89	22.06	22.70
TiO_2	0.05	0.00	0.07	0.04	0.06	0.06	0.00	0.02	0.01	0.06	0.00	0.01	0.02	0.02	0.00	0.00
FeO	25.04	26.21	24.77	26.43	25.75	23.73	27.85	27.87	24.31	26.61	25.00	25.53	27.10	26.47	23.28	24.27
MgO	13.53	13.38	14.32	12.63	13.24	14.04	12.20	12.45	13.90	14.75	13.85	12.66	13.16	12.76	13.81	13.78
CaO	0.10	0.03	0.05	0.05	0.05	0.12	0.01	0.10	0.06	0.07	0.06	0.16	0.02	0.01	0.05	0.04
MnO	0.31	0.14	0.22	0.31	0.37	0.31	0.84	0.62	0.37	0.37	0.39	0.38	0.37	0.37	0.32	0.43
Cr_2O_3	0.04	0.00	0.09	0.03	0.03	0.06	0.04	0.00	0.00	0.00	0.00	0.00	0.00	0.00	0.00	0.00
Na_2O	0.00	0.04	0.01	0.03	0.10	0.07	0.07	0.00	0.05	0.00	0.04	0.00	0.03	0.00	0.05	0.00
Total	87.17	88.25	88.94	85.75	86.92	86.76	87.62	87.25	86.55	87.57	87.65	85.43	87.52	87.01	84.33	86.16
14 oxygens																
Si	2.67	2.74	2.7	2.71	2.71	2.66	2.74	2.7	2.69	2.75	2.64	2.67	2.75	2.72	2.69	2.66
Al	2.84	2.76	2.82	2.73	2.75	2.88	2.66	2.68	2.82	2.5	2.87	2.83	2.64	2.76	2.83	2.86
Ti	0.01	0.00	0.01	0.01	0.01	0.01	0.00	0.00	0.00	0.01	0.00	0.00	0.00	0.00	0.00	0.00
Fe	2.22	2.3	2.14	2.40	2.30	2.10	2.50	2.51	2.16	2.37	2.2	2.32	2.42	2.37	2.12	2.17
Mg	2.13	2.09	2.20	2.05	2.11	2.21	1.95	2.00	2.20	2.34	2.17	2.05	2.09	2.03	2.24	2.19
Ca	0.01	0.01	0.01	0.01	0.01	0.02	0.08	0.01	0.01	0.04	0.01	0.02	0.00	0.00	0.01	0.01
Mn	0.03	0.01	0.02	0.03	0.04	0.03	0.08	0.06	0.04	0.04	0.04	0.04	0.04	0.04	0.03	0.04
Cr	0.01	0.00	0.01	0.00	0.00	0.01	0.01	0.00	0.00	0.00	0.00	0.00	0.00	0.00	0.00	0.00
Na	0.00	0.01	0.00	0.01	0.02	0.02	0.02	0.00	0.01	0.00	0.01	0.00	0.01	0.00	0.01	0.00
Total	9.90	9.90	9.89	9.93	9.92	9.90	9.94	9.96	9.91	10.01	9.93	9.92	9.94	9.91	9.91	9.92
XFe^{3+}	0.15	0.20	0.10	0.15	0.15	0.10	0.20	0.10	0.10	0.25	0.10	0.10	0.25	0.15	0.10	0.10
Error bar	2.90	1.22	6.91	2.90	7.34	4.70	3.01	4.68	5.77	4.15	7.27	7.92	0.01	3.50	3.51	5.10
T (°C)	390.40	316.14	358.65	366.60	348.87	406.95	361.24	418.35	397.13	362.32	434.82	414.12	337.00	349.56	393.33	418.69

Fiber II

Sample	CA20-12	CA20-13	CA20-17	CA20-19	CA18-118	CA18-123	CA18-124	CA20-10	CA20-11
SiO_2	26.74	27.11	27.12	27.19	27.27	27.62	26.56	27.06	26.57
Al_2O_3	18.70	18.05	18.46	19.47	18.85	18.60	22.00	18.45	18.07
TiO_2	0.03	0.02	0.02	0.00	0.03	0.00	0.03	0.00	0.07
FeO	23.54	23.26	23.67	19.91	21.49	21.53	22.03	23.77	23.82
MgO	17.79	17.71	17.19	19.32	17.14	17.92	14.14	18.06	18.15
CaO	0.09	0.11	0.18	0.09	0.09	0.01	0.04	0.07	0.06
MnO	0.23	0.18	0.18	0.65	0.54	0.37	0.30	0.23	0.15
Cr_2O_3	0.00	0.00	0.00	0.00	0.04	0.10	0.00	0.00	0.00
Na_2O	0.04	0.06	0.02	0.04	0.05	0.02	0.00	0.05	0.04
Total	87.15	86.49	86.82	86.67	85.49	86.15	85.08	87.70	86.94
14 oxygens									
Si	2.81	2.87	2.86	2.82	2.89	2.9	2.82	2.83	2.81
Al	2.32	2.25	2.3	2.38	2.36	2.31	2.76	2.28	2.25
Ti	0.00	0.02	0.00	0.00	0.00	0.00	0.00	0.00	0.01
Fe	2.07	2.06	2.09	1.73	1.91	1.89	1.96	2.08	2.11
Mg	2.79	2.8	2.71	2.99	2.71	2.81	2.24	2.82	2.86
Ca	0.01	0.01	0.02	0.01	0.01	0.00	0.01	0.01	0.01
Mn	0.02	0.02	0.02	0.06	0.05	0.04	0.03	0.02	0.02
Cr	0.00	0.00	0.00	0.00	0.01	0.01	0.00	0.00	0.00
Na	0.01	0.01	0.01	0.01	0.01	0.01	0.00	0.01	0.01
Total	10.03	10.01	9.99	9.99	9.94	9.95	9.80	10.04	10.07
XFe^{3+}	0.35	0.35	0.35	0.35	0.35	0.35	0.30	0.35	0.35
Error bar	30.03	26.05	22.85	22.57	27.16	30.42	2.76	14.47	13.89
T (°C)	316.28	266.97	259.26	312.50	233.7	229.51	273.72	297.60	338.55

Note: The temperature was calculated using the XFe^{3+} in the chlorites (Vidal et al., 2001, 2006). The error bar represents the scattering between the three reactions that can be written for the quartz-chlorite-water assemblage.
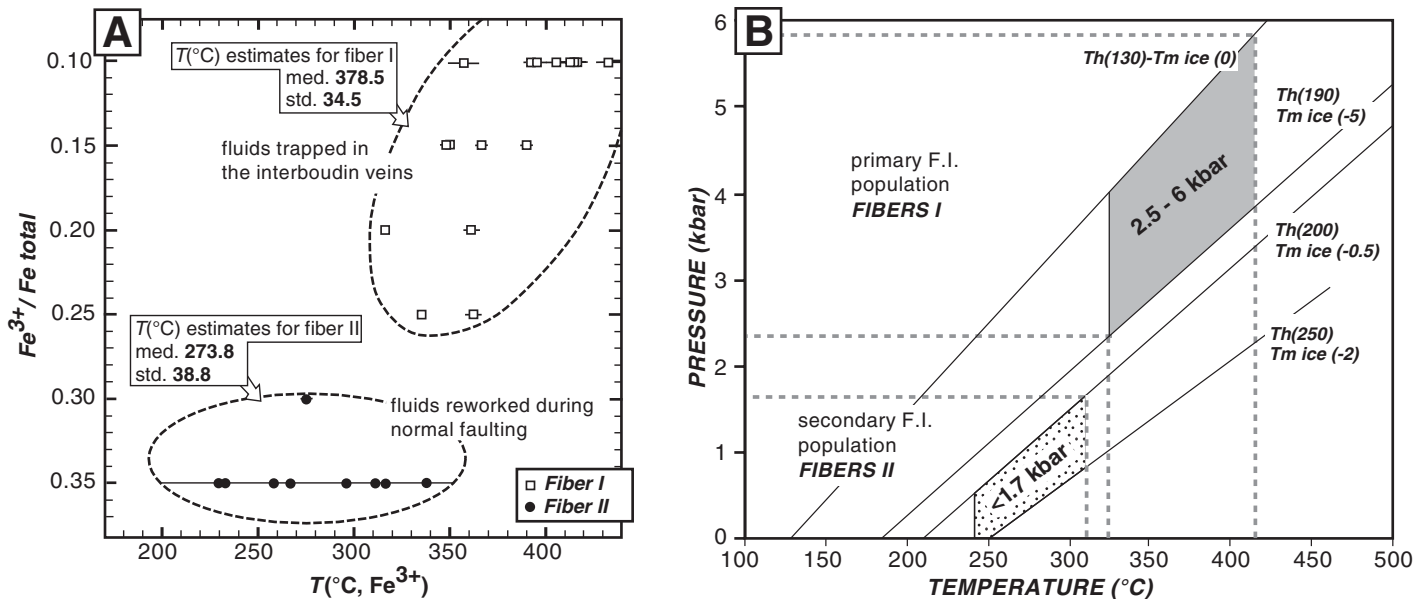
Figure 9. Pressure-temperature (*P-T*) calibration obtained by coupling chlorite composition and fluid inclusions (F.I.). **(A)** Estimates of the temperature during fiber formation, considering the proportion of Fe3+ in chlorites (Vidal et al., 2001, 2006). Median (med.) and standard deviation (std.) are indicated for each chlorite group (see data in Table 3). Error bars for each chlorite composition are presented; this error bar represents the scattering between the three reactions that can be written for the quartz-chlorite-water assemblage. Fiber I formed at a higher temperature than fiber II, which is associated with subsequent micronormal faulting. **(B)** *P-T* conditions during vein formation estimated by coupling the temperature formation of chlorites and the isochores calculated from fluid inclusions analyses of quartz fibers. Dotted areas locate the estimated *P-T* field for the boudinage process (fiber I) and for the subsequent faulting (fiber II). They are considered separately.

remained constant from the ductile-brittle transition (greenschist-facies conditions) up to the development of the present-day regional-scale normal faulting (Fig. 10). This tectonic regime is consistent with a subvertical orientation of the σ1 axis. Indeed, the latest normal faults indicate vertical σ1 axis orientation (Fig. 5C). However, in the present-day situation, we observe a finite geometry with (1) a west-dipping foliation plane and (2) a double boudinage geometry on the foliation plane and positions of microfaults compatible with a σ1 axis orientation steeply plunging toward the east (Figs. 4C and 5D).

In order to interpret these relationships between fixed orientation of σ1 axis and the present-day west-dipping regional structures (Fig. 3), we propose starting from a subhorizontal or low-angle attitude and westward rotation of the Schistes lustrés unit around a NNW-SSE horizontal axis during the boudinage to faulting sequence. In this hypothesis, the Schistes lustrés unit in its current position corresponds to an accretionary wedge tilted toward the west of more than 30° (Figs. 5 and 10). This tilting process allows the final exhumation to lead the metamorphic rocks toward the surface (Fig. 11A).

This interpretation has important consequences for kinematic analysis in the western Alps. For example, before being taken into account, all kinematic indicators developed under blueschist-facies conditions need to be restored to their original position (i.e., with a subhorizontal or gently dipping to the east position for the regional schistosity). This tilting was accommodated by west-dipping surfaces of extensional detachment parallel to the western flank of the Monviso and Dora-Maira massifs (Ballèvre et al., 1990) (Fig. 11B). These processes continued while the Queyras was exhumed from the ductile-to-brittle transition depth, up to the surface, during the Neogene (Tricart et al., 2004). The driving mechanism could have been the forethrusting of a 10-km-depth mantle indenter below the Dora-Maira massif in the east, which drove vertical compression and differential uplift of the internal Alpine units (Fig. 11C). This hypothesis is consistent with the lithospheric model proposed by Paul et al. (2001), Vernant et al. (2002), and Lardeaux et al. (2006), who imaged the so-called Ivrea geophysical body (Schmid and Kissling, 2000; Pfiffner et al., 2002).

CONCLUSION

The Queyras Schistes lustrés nappe stack represents a fossil accretionary wedge developed under blueschist-facies conditions during late Cretaceous–early Eocene subduction of the Tethyan ocean. The transition from subduction to collision is marked by a progressive evolution from ductile to brittle conditions of deformation in a global context of cooling from blueschist-greenschist to subsurface metamorphic conditions.

We focus here on the late tectonometamorphic evolution, from the mid-Oligocene onward: as collision continued, we demonstrate from microstructural observations that extension dominated. Synexhumation cooling caused the conditions of deformation to evolve from ductile, with the last crystallization of greenschist-facies minerals, to partly brittle with local boudinage, to finally fully brittle, with general normal faulting. During this final faulting stage, widespread small-scale faulting preceded the development of a major fault array at the regional scale. All along this second period, the tectonic regime was dominated by a major subvertical compression associated with subhorizontal multitiered, almost radial extension. It resulted in "chocolate tablet" double boudinage at the ductile-to-brittle transition and subsequently in normal faulting parallel and perpendicular to the general trend of the internal Alpine arc. These coeval, longitudinal and transverse faults remain currently
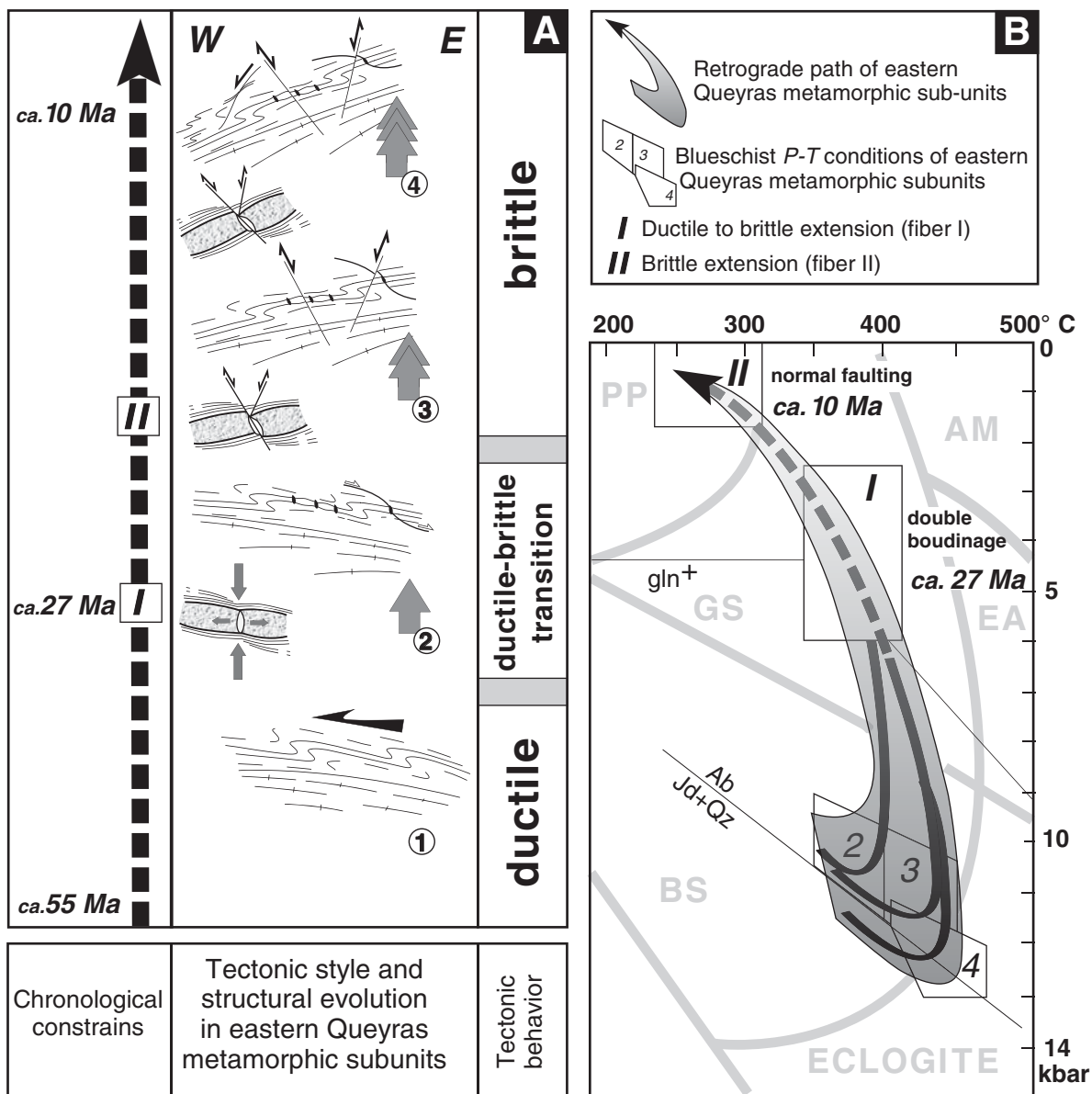
Figure 10. Structural and thermal history of the Schistes lustrés unit. (A) The deformation observed in the Queyras Schistes lustrés, along a W-E–oriented section, is interpreted in terms of successive stages of tilting: (1) Blueschist to greenschist ductile deformation is characterized by development of asymmetrical folds. (2) Ductile-to-brittle transition with development of "chocolate tablet" structures in competent (arkose, meta-basalt) beds generates veins between boudins (fiber I) and ductile normal faults in the enclosing calc-schist formations. (3) Brittle deformation is characterized by small-scale multitiered normal faulting. The previous boudin necks localized the nucleation of microfaults. The development of small-scale faults locally induced a rotation of the boudins. (4) Multiscale, multitiered normal faulting accompanied with final westward tilting. (B) In the pressure-temperature (*P-T*) diagram, fields I and II refer to the conditions of ductile to brittle extension (boudinage, fiber I) and to subsequent brittle extension (normal faulting, fiber II), respectively. Metamorphic facies are from Spear (1993) (see Fig. 2). The stability field of glaucophane (gln) (Maresch, 1977) and the reaction jadeite + quartz = albite (Holland, 1980) are indicated.
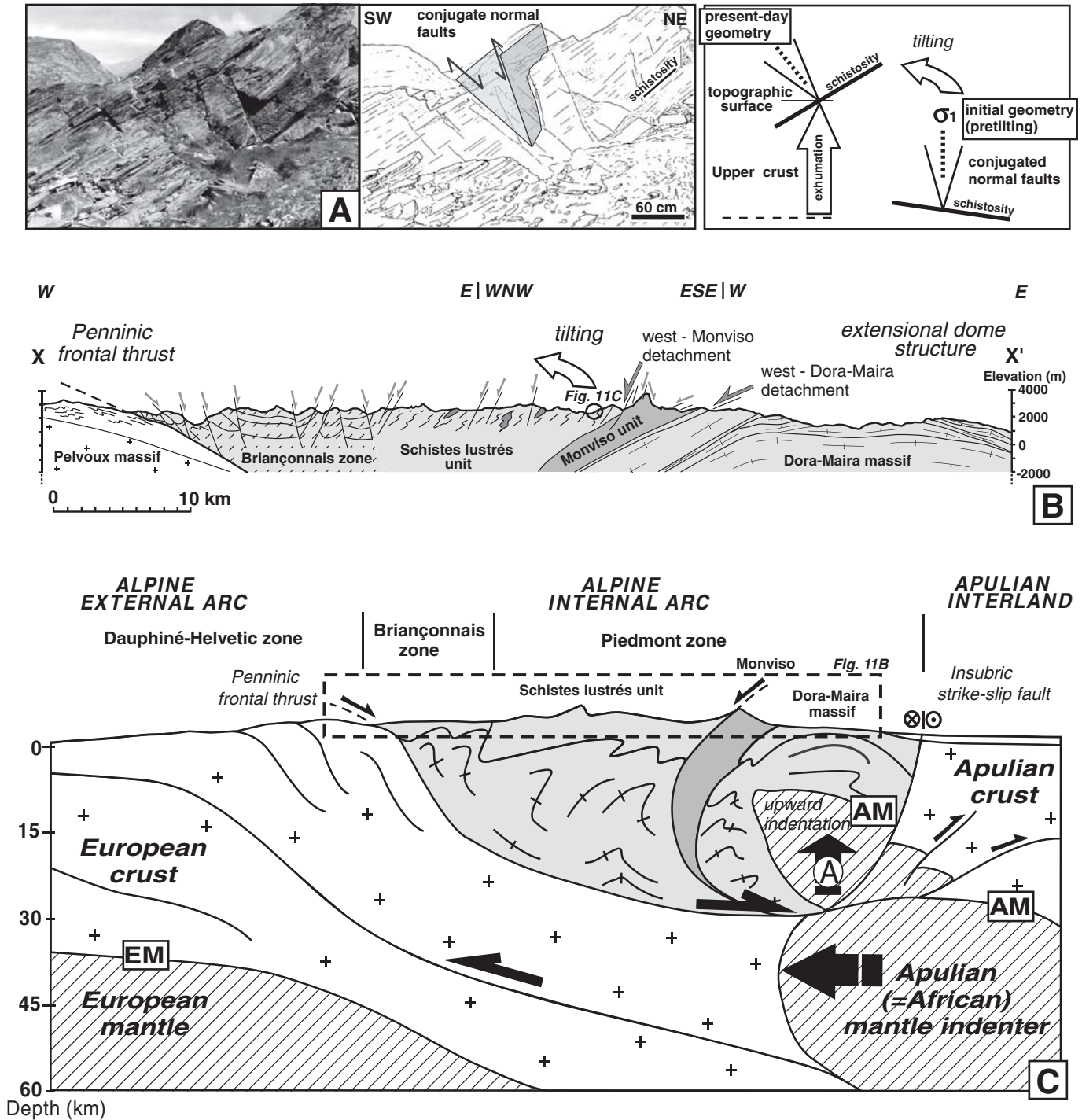
Figure 11. Multiscale interpretations across the western Alps. (A) Small-scale structures showing tilted conjugated normal faults in Queyras Schistes lustrés and the proposed interpretations. (B) X-X′ geological transect showing the Penninic deep crustal thrust to the west and the main detachments localized at the Schistes lustrés–Monviso and Monviso–Dora-Maira boundaries to the east. The present-day geometry of the Dora-Maira massif as an extensional dome structure is also compatible with vertical compression (modified after Tricart et al., 2004). (C) Crustal-scale section showing the depth of the European Moho (EM) and Apulian lithospheric mantle indenter (AM) from Paul et al. (2001) and Lardeaux et al. (2006). In response to plate convergence, the upper part of the Apulian (African) lithospheric mantle acts as an indenter responsible for up-doming in the Dora-Maira the massif and tilting of the Schistes lustrés unit (upward indentation: vertical arrow A). The present-day west-dipping attitude of the schistosity in the Schistes lustrés unit results from this regional-scale tilting. Coeval widespread normal faulting in the Briançonnais zone and Schistes lustrés unit is also consistent with a subvertical orientation of σ1.

active in the upper seismogenic crust, resulting in the regional seismicity. The subvertical compression from the mid-Oligocene onward has driven the progressive westward tilting of the Schistes lustrés and is associated with the development of west-dipping detachment faults along the Schistes lustrés–Monviso and along the Monviso–Dora-Maira boundaries.

In the Schistes lustrés, microtectonic analysis allowed discrimination of two generations of veins, one associated with boudinage and another with postboudinage normal faulting. The veins contain syntectonic quartz-chlorite-albite fibers, labeled I and II, respectively. Early interboudin veins (fiber I) developed at 380 ± 35 °C and 6–2.5 kbar, whereas en echelon veins (fiber II) associated with overprinted normal faults developed at 275 ± 40 °C and <1.7 kbar. Chronological milestones were given by recently published fission-track ages from zircons and apatites, suggesting that in the presently exposed units, the ductile-to-brittle transition occurred between ca. 27 Ma and ca. 10 Ma.

Two possible driving mechanisms for this multitiered extension have been proposed in the inner western Alps: gravitational collapse of the overthickened European crust (Sue et al., 2007) and upward indentation of the European crust by the Apulian mantle (Lardeaux et al., 2006). Evidence of extension associated with westward tilting of the Queyras Schistes lustrés nappe stack during late European-Africa convergence is more consistent with this second hypothesis. The Apulian mantle wedge has played a major role in the Alpine collision process (Schmid and Kissling, 2000; Pfiffner et al., 2002). Our "late Alpine" scenario proposed here in the core of the arc is consistent with the persistence of this deep indentation from the beginning of the Neogene onward.

REFERENCES CITED

Agard, P., Goffé, B., Touret, J.L.R., and Vidal, O., 2000, Retrograde mineral and fluid evolution in high-pressure metapelites (Schistes lustrés unit, western Alps): Contributions to Mineralogy and Petrology, v. 140, p. 296–315, doi: 10.1007/s004100000190.

Agard, P., Jolivet, L., and Goffé, B., 2001, Tectonometamorphic evolution of the Schistes lustrés complex: Implications for the exhumation of the HP and UHP rocks in the western Alps: Bulletin de la Société Géologique de France, v. 172, p. 617–636, doi: 10.2113/172.5.617.

Agard, P., Monie, P., Jolivet, L., and Goffé, B., 2002, Exhumation of the Schistes Lustrés complex: In situ laser probe Ar-40/Ar-39 constraints and implications for the western Alps: Journal of Metamorphic Geology, v. 20, p. 599–618, doi: 10.1046/j.1525-1314.2002.00391.x.

Angelier, J., 1990, Inversion of field data in fault tectonics to obtain the regional stress: A new rapid direct inversion method by analytical means: Geophysical Journal International, v. 103, p. 363–376, doi: 10.1111/j.1365-246X.1990.tb01777.x.

Ballèvre, M., Lagabrielle, Y., and Merle, O., 1990, Tertiary ductile normal faulting as a consequence of lithospheric ductile stacking in the western Alps: Mémoire de la Société Géologique de France 156, p. 227–236.

Beaumont, C., Jamieson, R.A., Nguyen, M.H., and Medvedev, S., 2004, Crustal channel flows: 1. Numerical models with applications to the tectonics of the Himalayan-Tibetan orogen: Journal of Geophysical Research, v. 109, p. B06406, doi: 10.1029/2003JB002809.

Belkin, H.E., 1994, Microthermometric investigations: Th and Tm practical and theoretical aspects, *in* De Vivo, B., and Frezzoti M.L., eds., Fluid Inclusions in Minerals: Methods and Applications: Blacksburg, Virginia, p. 7–23.

Blake, M.C., and Jayko, A.S., 1990, Uplift of very high pressure rocks in the western Alps: Evidence for structural attenuation along low angle faults, *in* Roure, F., Heitzmann, P., and Polino, R., eds., Deep structure of the Alps: Mémoire de la Société Géologique de France 156, p. 228–237.

Brix, M.R., Stöckhert, B., Seidel, E., Theye, T., Thomson, S.N., and Küster, M., 2002, Thermobarometric data from a fossil zircon partial annealing zone in high pressure–low temperature rocks of eastern and central Crete: Greece: Tectonophysics, v. 349, p. 309–326, doi: 10.1016/S0040-1951(02)00059-8.

Caby, R., 1996, Low-angle extrusion of high pressure rocks and the balance between outward and inward displacements of middle Penninic units in the western Alps: Eclogae Geologicae Helvetiae, v. 89, p. 229–267.

Caron, J.M., 1979, Relation entre métamorphisme et déformation dans les Alpes cottiennes: Eclogae Geologicae Helvetiae, v. 72, p. 497–506.

Chemenda, A.I., Mattauer, M., Malavieille, J., and Bokun A.N., 1995, A mechanism for syn-collisional rock exhumation and associated normal faulting: Results from physical modelling: Earth and Planetary Science Letters, v. 132, p. 225–232.

Chopin, C., Henry, C., and Michard, A., 1991, Geology and petrology of the coesite bearing terrain, Dora-Maira massif, western Alps: European Journal of Mineralogy, v. 3, p. 263–291.

Claudel, M.E., and Dumont, T., 1999, Early and Late Jurassic rifting events in the French Briançonnais relative to the evolution of the Ligurian Tethys and Valais oceans: Eclogae Geologicae Helvetiae, v. 92, p. 45–61.

Compagnoni, R., and Rolfo, F., 2003, UHPM units in the western Alps: European Mineralogy Union notes in Mineralogy, v. 5, p. 13–49.

Coward, M.P., and Dietrich, D., 1989, Alpine tectonics: An overview: Geological Society of London Special Publication 45, p. 1–29, doi: 10.1144/GSL.SP.1989.045.01.01.

Crawford, M.L., and Hollister, L.S., 1986, Metamorphic fluids: The evidence from fluid inclusions, *in* Walther, J.V., and Wood, B.J., eds., Fluid-Rock Interactions during Metamorphism. Advances in Physical Geochemistry: Berlin, Springer-Verlag, p. 1–35.

Deville, E., Fudral, S., Lagabrielle, Y., Marthaler, M., and Sartori, M., 1992, From oceanic closure to continental collision: A synthesis of the Schistes lustrés metamorphic complex of the western Alps: Geological Society of America Bulletin, v. 104, p. 127–139, doi: 10.1130/0016-7606(1992)104<0127:FOCTCC>2.3.CO;2.

Dewey, J., 1988, Extensional collapse of orogens: Tectonics, v. 7, p. 1123–1139, doi: 10.1029/TC007i006p01123.

Duchêne, S., Blichert-Toft, J., Luais, B., Télouk, P., Lardeaux, J.M., and Albarède, F., 1997, The Lu-Hf dating of garnets and the ages of the Alpine high-pressure metamorphism: Nature, v. 387, p. 586–589, doi: 10.1038/42446.

Durney, D.W., and Ramsay, J.G., 1973, Gravity and tectonics, *in* De Jong, K.A., and Scholten, R., eds., Gravity and tectonics: New York, Wiley, p. 67–96.

Faccenna, C., Becker, T.W., Lucente, F.P., Jolivet, L., and Rosetti, F., 2001, History of subduction and back arc extension in the central Mediterranean: Geophysical Journal Interiors, v. 145, p. 809–820, doi: 10.1046/j.0956-540x.2001.01435.x.

Ganne, J., Bertrand, J.M., and Fudral, S., 2005, Fold interference pattern at the top of basement domes and apparent vertical extrusion of HP rocks (Ambin and South Vanoise massifs, western Alps): Journal of Structural Geology, v. 27, p. 553–570, doi: 10.1016/j.jsg.2004.11.004.

Goffé, B., Schwartz, S., Lardeaux, J.M., and Bousquet, R., 2004, Explanatory notes to the map: Metamorphic structure of the Alps, western and Ligurian Alps: Mitteilungen der Osterreichischen Mineralogischen Gessellschaft, v. 149, p. 125–144.

Goscombe, B.D., and Passchier, C.W., 2003, Asymmetric boudins as shear indicator—An assessment from field data: Journal of Structural Geology, v. 25, p. 575–589, doi: 10.1016/S0191-8141(02)00045-7.

Goscombe, B.D., Passchier, C.W., and Hand, M., 2004, Boudinage classification: End-member boudins type and modified boudin structures: Journal of Structural Geology, v. 26, p. 739–763, doi: 10.1016/j.jsg.2003.08.015.

Gratier, J.P., Ménard, G., and Arpin, R., 1989, Strain-displacement compatibility and restoration of the Chaînes Subalpine of the western Alps: Geological Society of London Special Publication 45, p. 65–81, doi: 10.1144/GSL.SP>1989.045.01.04.

Hodges, K.V., Parrish, R.R., Housh, T.B., Lux, D.R., Burchfield, B.C., Royden, L.H., and Chen, Z., 1992, Simultaneous Miocene extension and shortening in the Himalaya orogen: Science, v. 258, p. 1466–1470, doi: 10.1126/science.258.5087.1466.

Holland, T.J.B., 1980, The reaction albite = jadeite +quartz determined experimentally in the range 600–1200°C: The American Mineralogist, v. 65, p. 129–134.

Jolivet, L., Monié, P., Truffert, C., Patriat, M., and Bonneau, M., 1996, Miocene detachment in Crete and exhumation *P-T-t* paths of high-pressure metamorphic rocks: Tectonics, v. 15, p. 1129–1153.

Lagabrielle, Y., and Polino, R., 1988, Un schéma structural du domaine des Schistes lustrés ophiolitifère au nord-ouest du massif du Mont Viso (Alpes Sud-Occidentales) et ses implications: Comptes Rendus de l'Académie des Sciences, v. 306, p. 921–928.

Lardeaux, J.M., Schwartz, S., Paul, A., Tricart, P., Guillot, S., Béthoux, N., and Masson, F., 2006, A crustal-scale cross section of the southwestern Alps combining geophysical and geological imagery: Terra Nova, v. 18, p. 412–422, doi: 10.1111/j.1365-3121.2006.00706.x.

Lemoine, M., Bas, T., Arnaud-Vanneau, A., Arnaud, A., Dumont, T., Gidon, M., Bourbon, M., de Graciansky, P.C., Rudkiewicz, J.L., Mégard-Galli, J., and Tricart, P., 1986, The continental margin of the Mesozoïc Tethys in the western Alps: Marine and Petroleum Geology, v. 3, p. 179–199, doi: 10.1016/0264-8172(86)90044-9.

Lombardo, B., Nervo, R., Compagnoni, R., Messiga, B., Kienast, J.R., Mével, C., Fiora, L., Piccardo, G.B., and Lanza, R., 1978, Osservazioni preliminari sulle ofiolite metamorfiche del Monviso (Alpi Occidentali): Rendi Conti Società Italiana di Mineralogia e Petrologia, v. 34, p. 253–305.

Lyon-Caen, H., and Molnar, P., 1989, Constraints on the deep structure and dynamic processes beneath the Alps and adjacent regions from an analysis of gravity anomalies: Geophysical Journal International, v. 99, p. 19–32, doi:10.1111/j.1365-246X.1989.tb02013.x

Malavieille, J., Guilhot, P., Lardeaux, J.M., and Gardien, V., 1990, Collapse of a thickened Variscan crust in the French Massif Central: Mont Pilat extensional shear zone and Saint-Etienne Upper-Carboniferous basin: Tectonophysics, v. 177, p. 139–149, doi: 10.1016/0040-1951(90)90278-G.

Maresch, W.V., 1977, Experimental study on glaucophane, an analysis on present knowledge: Tectonophysics, v. 43, p. 109–125, doi: 10.1016/0040-1951(77)90008-7.

Nicolas, A., Polino, R., Hirn, A., Nicolich, R., and ECORS-CROP Working Group, 1990, ECORS-CROP traverse and deep structure of the western Alps, *in* Roure, F., Heitzmann, P., and Polino, R., eds., Deep structure of the Alps: Mémoire de la Société Géologique 156, p. 15–27.

Paul, A., Cattaneo, M., Thouvenot, F., Spallarossa, D., Bethoux, N., and Frechet, J., 2001, A three-dimen-

sional crustal velocity model of the southwestern Alps from local earthquake tomography: Journal of Geophysical Research, v. 106, p. 19,367–19,389, doi: 10.1029/2001JB000388.

Pfiffner, O.A., Schlunegger, F., and Buiter, S.J.H., 2002, The Swiss Alps and their peripheral foreland basin: Stratigraphic response to deep crustal processes: Tectonics, v. 21, p. 1–17.

Philippot, P., 1990, Opposite vergence of nappes and crustal extension in the French-Italian Western Alps: Tectonics, v. 9, p. 1143–1164.

Platt, J.P., 1987, The uplift of high pressure–low temperature metamorphic rocks: Royal Society of London Philosophical Transactions, Series A, v. 321, p. 87–103, doi: 10.1098/rsta.1987.0006.

Pognante, U., and Kienast, J.R., 1987, Blueschist and eclogite transformation in Fe-Ti gabbros: A case from the western Alps ophiolites: Journal of Petrology, v. 28, p. 271–292.

Rahn, M., Brandon, M., Batt, G., and Garver, J., 2004, A zero-damage model for fission-track annealing in zircon: The American Mineralogist, v. 89, p. 473–484.

Ramsay, J.G., 1967, Folding and Fracturing of Rocks: New York, McGraw-Hill, 268 p.

Reiners, P.W., and Brandon, M.T., 2006, Using thermochronology to understand orogenic erosion: Annual Review of Earth and Planetary Sciences, v. 34, p. 419–466, doi: 10.1146/annurev.earth.34.031405.125202.

Ring, U., Bradon, M.T., Willet, S.D., and Lister, G.S., 1999, Exhumations processes: Geological Society of London Special Publication 154, p. 1–27, doi: 10.1144/GSL.SP.1999.154.01.01.

Roedder, E., 1984, Fluid inclusions, *in* Ribe, P.H., eds., Reviews in Mineralogy: Washington, D.C., Mineralogical Society of America, 644 p.

Rolland, Y., Lardeaux, J.M., Guillot, S., and Nicollet, C., 2000, Extension syn-convergence, poinçonnement vertical et unités métamorphiques contrastées en bordure Ouest du Grand Paradis (Alpes Franco-Italiennes): Geodinamica Acta, v. 13, p. 133–148, doi: 10.1016/S0985-3111(00)00111-X.

Rosenbaum, G., and Lister, G.S., 2005, The western Alps from the Jurassic to Oligocene: Spatio-temporal constraints and evolutionary reconstructions: Earth-Science Reviews, v. 69, p. 281–306, doi: 10.1016/j.earscirev.2004.10.001.

Rubatto, D., and Hermann, J., 2001, Exhumation as fast as subduction?: Geology, v. 29, p. 3–6, doi: 10.1130/0091-7613(2001)029<0003:EAFAS>2.0.CO;2.

Schmid, S.M., and Kissling, E., 2000, The arc of the western Alps in the light of geophysical data on deep crustal structure: Tectonics, v. 19, p. 62–85, doi: 10.1029/1999TC900057.

Schwartz, S., 2000. La Zone Piémontaise des Alpes Occidentales: Un Paléo-Complexe de Subduction [Ph.D. thesis]: Lyon, University of Lyon, 278 p.

Schwartz, S., Lardeaux, J.M., Guillot, S., and Tricart, P., 2000, Diversité du métamorphisme éclogitique dans le massif ophiolitique du Monviso (Alpes occidentales, Italie): Geodinamica Acta, v. 13, p. 169–188, doi: 10.1016/S0985-3111(00)00112-1.

Schwartz, S., Allemand, P., and Guillot, S., 2001, Numerical model of the effect of serpentinites on the exhumation of eclogitic rocks: Insights from the Monviso ophiolitic massif (Western Alps): Tectonophysics, v. 342, p.193–206.

Schwartz, S., Lardeaux, J.M., Tricart, P., Guillot, S., and Labrin, E., 2007, Diachronous exhumation of HP-LT metamorphic rocks from southwestern Alps: Evidence from fission-track analysis: Terra Nova, v. 19, no. 2, p. 133–144, doi: 10.1111/j.1365-3121.2006.00728.x.

Selverstone, J., 2005, Are the Alps collapsing?: Annual Review of Earth and Planetary Sciences, v. 33, p. 113–132, doi: 10.1146/annurev.earth.33.092203.122535.

Shepherd, T.J., Rankin, A., and Alderton, D., 1985, A Practical Guide to Fluid Inclusion Studies: London, Chapman and Hall, 239 p.

Spear, F.S., 1993, Metamorphic phase equilibria and pressure-temperature-time paths: Washington, D.C., Mineralogical Society of America, 799 p.

Sue, C., and Tricart, P., 2003, Neogene to ongoing normal faulting in the inner western Alps: Tectonics, v. 5, p. 1–25.

Sue, C., Thouvenot, F., Fréchet, J., and Tricart, P., 1999, Widespread extension in the core of the western Alps revealed by earthquake analysis: Journal of Geophysical Research, v. 104, p. 25,611–25,622, doi: 10.1029/1999JB900249.

Sue, C., Martinod, J., Tricart, P., Thouvenot, F., Gamond, J.F., Frechet, J., Marinier, D., Glot, J.P., and Grasso, J.R., 2000, Active deformation in the inner western Alps inferred from comparison between 1972-classical and 1996-GPS geodetic surveys: Tectonophysics, v. 320, p. 17–29, doi: 10.1016/S0040-1951(00)00024-X.

Sue, C., Delacou, B., Champagnac, J.D., Allanic, C., Tricart, P., and Burkard, M., 2007, Extensional neotectonics around the bend of the western/central Alps: An overview: International Journal of Earth Sciences, v. 96, p. 1101–1129, doi: 10.1007/s00531-007-0181-3.

Tricart, P., 1984, From passive margin to continental collision: A tectonic scenario for the western Alps: American Journal of Science, v. 284, p. 97–120.

Tricart, P., and Lemoine, M., 1986, From faulted blocks to megamullions and megaboudins—Tethyan heritage in the structure of the western Alps: Tectonics, v. 5, p. 95–118, doi: 10.1029/TC005i001p00095.

Tricart, P., and Schwartz, S., 2006, A north-south section across the Queyras Schistes lustrés (Piedmont zone, western Alps): Syn-collision refolding of a subduction wedge: Eclogae Geologicae Helvetiae, v. 99, p. 429–442, doi: 10.1007/s00015-006-1197-6.

Tricart, P., Schwartz, S., Sue, C., Poupeau, G., and Lardeaux, J.M., 2001, La dénudation tectonique de la zone ultradauphinoise et l'inversion du front Briançonnais au sud-est du Pelvoux (Alpes occidentales): Une dynamique Miocène à actuelle: Bulletin de la Société Géologique de France, v. 172, p. 49–58, doi: 10.2113/172.1.49.

Tricart, P., Amauric Du Chaffaut, S., Ayoub, C., Ballèvre, M., Caby, R., Gout, C., Lagabrielle, Y., Leblanc, D., Le Mer, O., Philippot, P., and Saby, P., 2003, Carte géologique de France: Feuille Aiguilles–Col Saint Martin (848): Orléans, Bureau de Recherches Géologiques et Minières, scale 1:50,000.

Tricart, P., Schwartz, S., Sue, C., and Lardeaux, J.M., 2004, Differential exhumation in the inner western Alpine arc evidenced by late normal faulting (eastern Queyras Schistes lustrés): Journal of Structural Geology, v. 26, p. 1633–1645, doi: 10.1016/j.jsg.2004.02.002.

Tricart, P., Lardeaux, J.M., Schwartz, S., and Sue, C., 2006, The late extension in the inner western Alps: A synthesis along the south-Pelvoux transect: Bulletin de la Société Géologique de France, v. 6, p. 299–310.

Vernant, P., Masson, F., Bayer, R., and Paul, A., 2002, Sequential inversion of local earthquake traveltimes and gravity anomaly—The example of the western Alps: Geophysical Journal International, v. 150, p. 79–90, doi: 10.1046/j.1365-246X.2002.01694.x.

Vidal, O., Parra, T., and Trotet, F., 2001, A thermodynamic model for Fe-Mg aluminous chlorite using data from phase equilibrium experiments and natural pelitic assemblages in the 100–600°C, 1–25 kbar *P-T* range: American Journal of Science, v. 301, p. 557–592, doi: 10.2475/ajs.301.6.557.

Vidal, O., Parra, T., and Vieillard, P., 2005, Thermodynamic properties of the Tschermak solid solution in Fe-chlorite: Application to natural examples and possible role of oxidation: The American Mineralogist, v. 90, p. 347–358, doi: 10.2138/am.2005.1554.

Vidal, O., DeAndrade, V., Lewin, E., Munoz, M., Parra, T., and Pascarelli, S., 2006, *P-T*-deformation-Fe3+/Fe2+ mapping at the thin section scale and comparison with XANES mapping: Application to a garnet-bearing metapelite from the Sambagawa metamorphic belt (Japan): Chemical Geology, v. 64, p. 335–350.

Zhang, Y., and Frantz, J.D., 1987, Determination of homogeneous temperatures and densities of supercritical fluids in the system NaCl-KCl-CaCl2–H2O using synthetic fluid inclusions: Geology, v. 64, p. 335–350, doi: 10.1016/0009-2541(87)90012-X.